J. Fluid Mech. (2023), *vol*. 955, A10, doi:10.1017/jfm.2022.1051

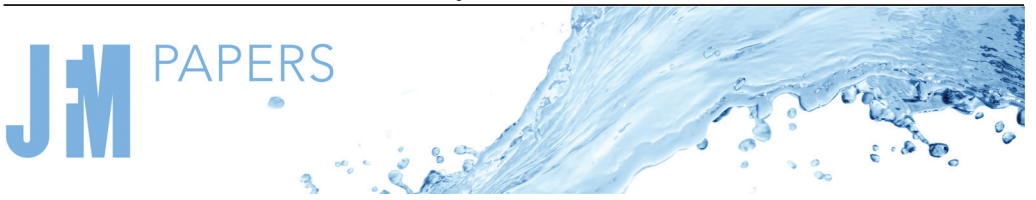

Activity-induced migration of viscous droplets on a solid substrate

A. Aggarwal[1,2], **E. Kirkinis**[1,2,†] **and M. Olvera de la Cruz**[1,2]

[1]Department of Materials Science & Engineering, Robert R. McCormick School of Engineering and Applied Science, Northwestern University , Evanston IL 60208, USA

[2]Center for Computation and Theory of Soft Materials, Northwestern University, Evanston IL 60208, USA

(Received 26 April 2022; revised 14 November 2022; accepted 7 December 2022)

Active matter exploits motion to induce changes in shape and conformation via external input. In this paper, we establish theoretically that viscous liquid droplets containing magnetic nanoparticles with frozen-in magnetic moments, sitting on a solid substrate and surrounded by an ambient gas phase, can deform and migrate under the influence of a magnetic torque. The effect arises because the collective rotation of the magnetic nanoparticles at the liquid–gas interface tilts the droplet away from a symmetric configuration, breaks the reflection symmetry with respect to the centre axis, and leads to a left–right asymmetry of the contact angles. A sufficiently strong magnetic torque leads the contact angles to overcome hysteresis effects leading the droplet to migrate. We develop a general framework to explain how symmetry-breaking affects droplet migration. Thus previous results of droplet spreading and migration can be recovered as special cases. Such droplets can be employed as agents in active surfaces and can move against gravity, chemical and thermal gradients, providing a mechanism that could be utilized by both industry and medicine.

Key words: thin films, lubrication theory

1. Introduction

In recent years, it has become possible to design and synthesize systems that execute cooperative functions employing active matter; cf. Driscoll & Delmotte (2019) and references therein. Active materials are controlled by the application of external inputs such as chemical energy, magnetic fields and/or light. Because magnetic fields can penetrate matter, they can replace chemical energy in actuating systems by enabling, for instance, the locomotion of robots (Li *et al.* 2020; Yang *et al.* 2020).

† Email address for correspondence: kirkinis@northwestern.edu

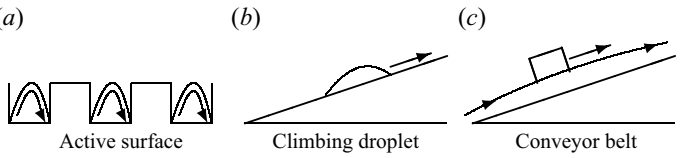

Figure 1. Possible applications of the present formalism. (*a*) Active surfaces: active droplets embedded in the grooves of a solid surface reduce hysteresis and increase mobility. Arrows indicate streamlines and flow direction. (*b*) Active droplets: they can squeeze through narrow spaces, work against gravitational potentials, temperature or chemical gradients, and overcome barriers (see § 5). Here they work against gravity climbing an inclined barrier. (*c*) Active films: they can be employed to transport cargo in a 'conveyor-belt' manner (see § 6).

Droplets of a magnetic liquid that can be actuated by external fields form a special case of active matter, which is employed in various fields of medicine and industry (Torres-Díaz & Rinaldi 2014). In particular, such droplets can be employed to form 'active surfaces' (cf. figure 1*a*) whereby they are placed in grooves of a surface and with the application of an external field they can reduce hysteresis effects and increase mobility (Torres-Díaz & Rinaldi 2014). Such droplets can: navigate uncharted terrains; climb an inclined plane working against pressure, thermal or chemical gradients and gravity (cf. figure 1*b*); move on the underside of a plate; climb and get past obstacles and even deform to enter narrow passageways (Torres-Díaz & Rinaldi 2014). Films composed of such a liquid can act as 'conveyor belts' for the transport of cargo (cf. figure 1*c*).

In this paper, we develop models capturing the motion of magnetic droplets in diverse terrains employing continuum field theories incorporating antisymmetric and couple stresses. Droplet motion as a whole – termed migration in this paper – depends on processes taking place at the contact line. Thus a brief discussion of known facts regarding the mobility of a contact line has a place here. It is a known experimental result (Dussan 1979) that a contact line moves with horizontal velocity u_{CL} according to

$$u_{CL} = k\left[\theta(t) - \bar{\theta}_A\right]^m, \quad \text{when } \theta(t) > \bar{\theta}_A, \tag{1.1}$$

where $\bar{\theta}_A \geqslant 0$ is the static advancing contact angle that $\theta(t)$ (the dynamic contact angle) has to overcome for the contact line motion to commence. The exponent m has been found in the experiments of Schwartz & Tejada (1972), Hoffman (1975) and Tanner (1979) to acquire the value $m = 3$. The phenomenological constant k also has to be determined by experiment. For instance, Ehrhard (1993) determined that $k \sim 4$ mm s^{-1} for silicon oil and $k \sim 8$ mm s^{-1} for paraffin oil in experiments of non-isothermal spreading on glass surfaces. For the receding contact angle of figure 2 (upper right), one has

$$u_{CL} = -k\left[\theta(t) - \bar{\theta}_R\right]^m, \quad \text{when } \theta(t) < \bar{\theta}_R, \tag{1.2}$$

where $\bar{\theta}_R \geqslant 0$ is the static receding contact angle that $\theta(t)$ (the dynamic contact angle) has to fall against for the contact line motion to commence. As discussed by Ehrhard & Davis (1991), there are a number of approaches to model the contact line dynamics. The first, termed the excision approach, uses lubrication theory to describe the bulk liquid flow away from the contact line. The excised contact-line region is then replaced by *a priori* statements about the drop shape and the 'outer' region (Tanner 1979; Ngan & Dussan V 1989). A second approach is to replace the contact line by a precursor film (de Gennes 1985). And a third is to consider the whole drop, introduce the constitutive law (1.1) and (1.2) at the contact line, and employ lubrication theory for flat drops (Greenspan 1978).

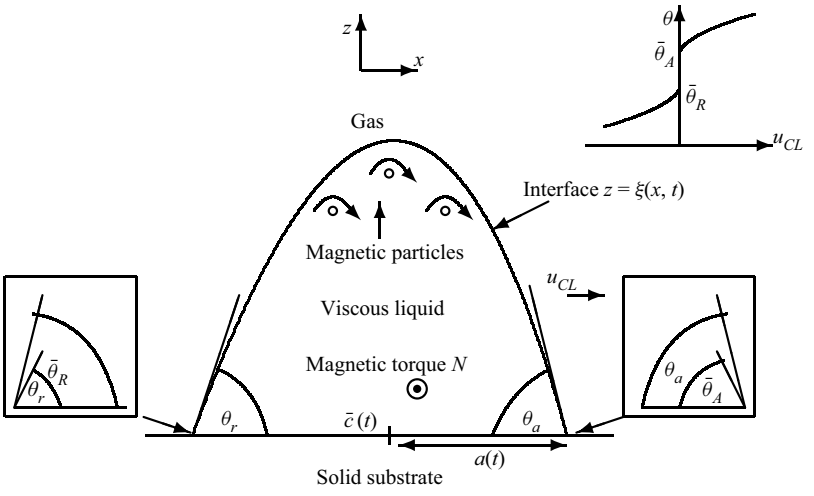

Figure 2. Top right: experiment-inspired hysteretic diagram of a single contact line moving with velocity u_{CL} versus dynamic contact angle θ (cf. (1.1) and Dussan 1979). Thus motion of the contact line takes place when the contact angle lies outside the interval $[\bar{\theta}_R, \bar{\theta}_A]$, determined by the static advancing and receding contact angles $\bar{\theta}_A$ and $\bar{\theta}_R$, respectively. Main figure: viscous droplet with rotational degrees of freedom (suspended ferromagnetic nanoparticles) sitting on a solid substrate and surrounded by an ambient gas phase. A moving interface at $z = \xi(x, t)$ separates a gas from a viscous liquid lying on a solid substrate located at $z = 0$. Nanosize particles suspended in the carrier liquid rotate with a macroscopic angular velocity field $\boldsymbol{\omega} = \omega(x, z, t)\,\hat{\boldsymbol{y}}$ by responding to a magnetic torque density $N\hat{\boldsymbol{y}} = \boldsymbol{m} \times \boldsymbol{h}$ produced by a rotating magnetic field of frequency ν applied on the suspension of macroscopic magnetization $\boldsymbol{m}$. The particle collective rotation near the liquid–gas interface induces a dominant horizontal liquid velocity component $u(x, z, t)\,\hat{\boldsymbol{x}}$ deforming the droplet, tilting it to the right. If the torque is strong enough so that the droplet overcomes hysteresis effects (and thus the left dynamic contact angle $\theta_r(t)$ falls short of the receding static angle $\bar{\theta}_R$, and the right dynamic contact angle $\theta_r(t)$ exceeds the advancing static contact angle $\bar{\theta}_A$ – see the corresponding insets), then it starts moving to the right with velocity u_{CL}.

This latter approach was employed successfully by Ehrhard & Davis (1991) to develop a theory of thermocapillary spreading, validated by subsequent experiments (Ehrhard 1993) and by Smith (1995) to study the migration of liquid droplets under a horizontal temperature gradient. In the spreading case of Ehrhard & Davis (1991), a vertical temperature gradient gives rise to surface tension variations that are symmetric with respect to the centre axis of the droplet, and leads to the formation of two symmetric flow cells inside the droplet (cf. Ehrhard & Davis 1991, figure 5), even when spreading has ceased. In this spreading regime, the contact lines always remain equal and the droplet shape stays symmetric with respect to its centre axis. On the other hand, a horizontal temperature gradient gives rise to asymmetric surface tension with respect to the centre axis of the droplet. The corresponding surface tension gradient tilts the droplet and gives rise, in principle, to a single cell (Smith 1995, figure 6), and drives these non-isothermal droplets to migrate. During migration, the left and right contact angles (cf. figure 2) are unequal, and the shape of the droplet is asymmetric with respect to its centre axis. It is interesting to note that the effect of the horizontal temperature gradient (subject to certain approximations employed by Smith 1995) on the liquid–gas interface is equivalent to the one that would be generated by a constant surface shear 'wind' imposed on a droplet or film (Davis, Gratton & Davis 2010).

In this paper, we follow the third approach, based on the constitutive law (1.1) and (1.2), validated by experiment (Schwartz & Tejada 1972; Hoffman 1975; Tanner 1979).

It is perhaps important to point out here that the quasi-static migration droplet profiles of Ehrhard & Davis (1991) and Smith (1995) were obtained by a perturbation approach, whereby the external field (a vertical or horizontal temperature gradient, respectively) was superposed as a perturbation on a basic state determined by gravity and surface tension. In contrast, in the present paper, we obtain, theoretically, quasi-static migration profiles exactly, that is, with a non-perturbative approach.

Migration is realized when both dynamic contact angles overcome their advancing and receding static counterparts, i.e. when the right dynamic contact angle $\theta_a(t)$ exceeds the static advancing contact angle $\bar{\theta}_A$, and the left dynamic contact angle $\theta_r(t)$ falls short of the static receding contact angle $\bar{\theta}_R$ (cf. figure 2). For the problem under consideration, notation becomes increasingly cumbersome. With a view to simplify it, we adopt the notation employed by Smith (1995) and Ehrhard & Davis (1991). We are interested mainly in the steady-state regime, that is, when the droplet has acquired a constant migration velocity, specific shape and constant radius. Initial and transient behaviour is of some interest, and this have been discussed in detail by Smith (1995) for the thermocapillary problem under a horizontal temperature gradient.

Fine ferromagnetic particles suspended in a Newtonian liquid can bring about an imbalance of angular momentum (Dahler & Scriven 1961; Condiff & Dahler 1964; Rinaldi 2002). This imbalance is due to deviations of the macroscopic particle angular velocity from the liquid angular velocity, that is, one-half of the liquid's vorticity field, generated by an external magnetic field.

A magnetic torque can drive the suspended particles in such a way that at the liquid–gas interface, their collective rotation (in a 'conveyor-belt fashion', see figure 2) described by the macroscopic particle angular velocity $\boldsymbol{\omega}$ (Rinaldi 2002) manifests itself as an effective, non-uniform surface shear stress. The effect of such a stress is to provide a dominant component tangential to the liquid–gas interface for the fluid velocity $\boldsymbol{u}$, which causes a droplet to deform.

In this paper, we establish theoretically that viscous liquid droplets containing magnetic nanoparticles with frozen-in magnetic moments, sitting on a solid substrate and surrounded by an ambient gas phase, can migrate under the influence of a magnetic torque generated by a rotating magnetic field (cf. figure 2). The effect arises because the collective rotation of the magnetic nanoparticles at the liquid–gas interface tilts the droplet away from a symmetric configuration, breaks the reflection symmetry with respect to the centre axis, and leads to a left–right asymmetry of the contact angles (cf. insets of figure 2). A sufficiently strong magnetic torque leads the contact angles to overcome hysteresis effects and induces droplet migration. Thus this is a symmetry-breaking effect at the level of the Navier–Stokes equations. Symmetry-breaking is also inherited by the liquid–gas profile evolution equation as well as the mobility constitutive law (1.1) and (1.2) describing the motion of a contact line. The effect is a companion to the thermocapillary migration of the non-isothermal liquid droplets analysed theoretically by Smith (1995). Thus the theoretical framework developed in the present paper, with respect to symmetry-breaking and droplet mobility, encompasses these former results as special cases.

The paper is organized as follows. In § 2, we outline the theory of liquids with rotational degrees of freedom that embodies the balance of internal angular momentum of suspended particles through their macroscopic angular velocity $\boldsymbol{\omega}$. It is important to note that the conditions that couple stresses satisfy on a free surface of such a liquid were derived only recently by Chaves & Rinaldi (2014). This point as well as other interfacial conditions are discussed in § 2.1.

The reduction of the full Navier–Stokes and angular momentum equations in the geometry displayed in figure 2 is described in detail in § 3. Allowance is made for a body force potential originating from a gravitational field. Such a potential can squeeze a droplet, leading to spreading, but it can also act in an accelerating or decelerating manner if the droplet migrates on an inclined substrate. A body force of magnetic origin is not included explicitly in this discussion as its effects are subdominant to their magnetic torque counterpart; cf. Kirkinis (2017). The reduction continues further in § 3.1 by resorting to the small initial contact angle (thin droplet) approximation (Ehrhard & Davis 1991; Smith 1995). The flow, driven by a time-averaged constant torque, leads to the generation of new nonlinear terms in the evolution equation for the liquid–gas interface of the droplet. To understand their physical significance, the asymptotic limit of vanishing film thickness is considered, which brings to prominence new convective terms of magnetic origin in the evolution equation.

In the ensuing sections, we will be taking the limit of small capillary number (§ 4.1 onwards), which provides a non-perturbative derivation of the liquid–gas interface (subject to the aforementioned approximations) away from an initial layer. In § 4, we calculate the migration velocity and the magnitude of the magnetic torque required to induce the mobility of the droplet. Possible effects of rotational slip (that is, finite particle angular velocity at the liquid–solid interface) are examined. Rotational slip favours migration, as velocity slip favours nonlinear wave propagation (Kirkinis 2017). It is interesting that all observables in this case can be expressed with respect to the capillary length, which determines the regime where gravity becomes important, through a Langevin function. Thus varying the capillary length, we can obtain the shape and velocity of droplets in various regimes. Numerical simulations of the piecewise mobility law embodied in (1.1) and (1.2) show the existence of a fixed point of both the droplet radius and its migration velocity, which are independent of initial data. Excellent agreement is established with our theoretical calculations of contact line velocity during the migration stage.

In § 5, we show that droplets can work against the potential of fields, here the gravitational field. Thus such a droplet can climb an inclined plane if the strength of the magnetic torque exceeds a certain limit. In § 6, we show that our theory also applies to the case of films climbing an inclined substrate. This case would be of interest for cargo transport in a conveyor-belt manner; see figure 1(*c*). We thus calculate the velocity of transport for the two aforementioned cases of zero and non-zero particle angular velocity at the liquid–solid interface.

Droplet migration is induced by symmetry-breaking. In § 7, we show how symmetry-breaking in the Navier–Stokes equations is inherited by the liquid–gas profile evolution equation and by the mobility law (1.1) and (1.2). Thus previous behaviours of thermocapillary spreading (Ehrhard & Davis 1991) or thermocapillary droplet migration (Smith 1995) can be recovered as special cases of our analysis.

In § 8, we provide estimates of the magnitude of the physical phenomena discussed in this paper based on standard experimental data available in the literature.

We conclude this paper in § 9 with a discussion of how the present framework could, in principle, be generalized to include effects that were met only recently in experiment (Ganeshan & Abanov 2017).

The inspiration of this problem originates from medicine, and in particular in how it would be possible to invent new and unconventional strategies for locomotion and thus therapy. We thus end this section with a discussion of targeting-specific locomotion strategies. In Appendix B, we develop a general framework that is valid when the

mechanism leading to spreading (Ehrhard & Davis 1991) or migration (Smith 1995) is superposed as a perturbation on a basic state. Thus previous perturbative results (Ehrhard & Davis 1991; Smith 1995) are recovered as special cases of this framework. In fact, in the small magnetic torque limit, our non-perturbative results can also be reduced and captured by this general (but perturbative) framework.

Although only suspensions of ferromagnetic particles driven by a magnetic field are considered in this paper, analogous arguments can be applied to the case of particles endowed with an electric dipole moment and acted upon by an electric field.

2. Viscous liquid motion in the presence of rotational degrees of freedom

In a liquid with rotational degrees of freedom – a classical Newtonian liquid with small suspended particles that can respond to an external torque – the balance of linear and internal angular momentum can be expressed in the form (Dahler & Scriven 1961; Condiff & Dahler 1964)

$$\rho\,\mathrm{D}u_i/\mathrm{D}t = \partial_k\sigma_{ik} \quad \text{and} \quad I\,\mathrm{D}\omega_i/\mathrm{D}t = \partial_k C_{ik} + N_i + \epsilon_{imk}\sigma_{km}, \quad i,k,m = 1,2,3, \tag{2.1a,b}$$

where $\mathrm{D}/\mathrm{D}t$ is the convective derivative, ρ is the fluid density, I is the volume density of particle moment of inertia, u_i is the fluid velocity, ω_i is the particle angular velocity, and N_i is the magnetic torque density. As noted by Dahler & Scriven (1961), the last term of (2.1b) represents the transformation of moment of momentum $\epsilon_{ijk}x_iu_j$ into internal angular momentum only when the stress σ_{ij} has an antisymmetric part. This part augments the standard Cauchy stress tensor and arises solely due to the inclusion of the nanostructure in the liquid. The resulting total stress $\boldsymbol{\sigma}$ is (Rinaldi 2002)

$$\sigma_{ik} = -p\delta_{ik} + \eta\hat{V}_{ik} + \zeta\,\hat{W}_{ik} + \hat{T}_{ik}, \tag{2.2}$$

where $\hat{V}_{ik} = \partial_k u_i + \partial_i u_k$ is twice the rate-of-strain tensor, $\hat{W}_{ik} = \partial_k u_i - \partial_i u_k - 2\epsilon_{kil}\omega_l$ is a 'spin' tensor measuring the imbalance between liquid and particle angular velocity, $\hat{T}_{ik} = (h_i b_k - \frac{1}{2}h_j^2\delta_{ik})/4\pi$ is the Maxwell stress tensor, and $\boldsymbol{h}$ and $\boldsymbol{b}$ denote the macroscopic magnetic field and induction, respectively. The liquid is considered incompressible

$$\partial_i u_i = 0, \tag{2.3}$$

p is the hydrostatic pressure, and η is the liquid viscosity. The phenomenological coefficient ζ multiplying $\hat{W}$ in (2.2) is termed the vortex viscosity in the literature (Condiff & Dahler 1964; Rinaldi 2002); ϵ_{ijk} is the alternating pseudo-tensor, and we employed the Einstein summation convention on repeated indices; $\hat{W}$ has curl $\boldsymbol{u} - 2\boldsymbol{\omega}$ as its axial vector. When this vector vanishes identically in the body of a slowly flowing viscous liquid in the absence of externally applied torques and non-conservative forces, the balance of internal angular momentum in (2.1a,b) is satisfied automatically, and the balance of linear momentum in (2.1a,b) reduces to the standard Navier–Stokes equations satisfied by the velocity field of an unstructured liquid (Condiff & Dahler 1964). Diffusion of internal angular momentum takes place due to couple stresses $\boldsymbol{C}$, where

$$C_{ik} = \eta'\,(\partial_k\omega_i + \partial_i\omega_k) + \zeta'\,\partial_j\omega_j\,\delta_{ik}, \tag{2.4}$$

that the suspended particles experience in their rotational motion. Here, η' and ζ' are the shear and bulk coefficients of spin viscosity (Condiff & Dahler 1964). Therefore, $\partial_j C_{ij}$ in

(2.1*a*,*b*) is the rate of arrival of internal angular momentum by way of diffusion. Maxwell's equations are

$$\nabla \times \boldsymbol{h} = \boldsymbol{0} \quad \text{and} \quad \nabla \cdot \boldsymbol{b} = 0, \tag{2.5a,b}$$

where $\boldsymbol{b} = \boldsymbol{h} + 4\pi\boldsymbol{m}$. Since the torque density

$$\boldsymbol{N} = \boldsymbol{m} \times \boldsymbol{h} \tag{2.6}$$

depends on the macroscopic magnetization field $\boldsymbol{m}$ of suspended particles, one more constitutive equation describing the evolution of this field has to be imposed in order to provide closure (Rinaldi 2002). This is

$$\mathrm{D}m_i/\mathrm{D}t = \epsilon_{ijk}\omega_j m_k - (m_i - \chi h_i)/\tau_B, \quad i = 1, 2, 3. \tag{2.7}$$

Here, τ_B is the Brownian relaxation time (Rinaldi 2002, pp. 54–57) and χ is the effective magnetic susceptibility:

$$\chi = n m_d L(\alpha)/h, \quad L = \coth\alpha - \frac{1}{\alpha}, \quad \alpha = \frac{m_d h}{k_B T}, \tag{2.8a–c}$$

where $m_d = M_d V$ is the magnetic moment of a single subdomain particle, V is the particle volume, M_d is the domain magnetization of dispersed ferromagnetic material, and n is the number density of the magnetic grains. In this form, (2.7) applies only at moderate strengths of the applied field. For a discussion of this point, see Rinaldi (2002, pp. 54–57) and references therein.

2.1. *Boundary conditions*

At a liquid–gas interface with mean curvature $\mathcal{K}$ and constant surface tension γ, continuity of traction implies (Oron, Davis & Bankoff 1997)

$$-[[\boldsymbol{\sigma}\boldsymbol{n}]] + 2\mathcal{K}\gamma\boldsymbol{n} = \boldsymbol{0}, \tag{2.9}$$

where $\boldsymbol{n}$ and $\boldsymbol{t}$ are the normal and tangent unit vectors at this interface, respectively, and the symbol $[[\cdot]]$ denotes the jump of the field across an interface. Thus for the shear and normal stresses, we have

$$[[\boldsymbol{t}\boldsymbol{\sigma}\boldsymbol{n}]] = 0 \quad \text{and} \quad [[\boldsymbol{n}\boldsymbol{\sigma}\boldsymbol{n}]] = 2\mathcal{K}\gamma, \tag{2.10a,b}$$

on the liquid–gas interface, while the couple stress tensor $\boldsymbol{C}$ satisfies (Chaves & Rinaldi 2014)

$$[[\boldsymbol{C}\boldsymbol{n}]] = \boldsymbol{0}. \tag{2.11}$$

At the liquid–solid interface, the no-slip and no-penetration conditions read

$$\boldsymbol{u} \cdot \boldsymbol{t} = 0, \quad \boldsymbol{u} \cdot \boldsymbol{n} = 0, \tag{2.12a,b}$$

respectively. When required, the former can be relaxed and be replaced by a slip model as is usual in thin liquid film and droplet studies (Oron *et al.* 1997; Kirkinis & Davis 2013, 2014). Finally, the question arises as to the most suitable boundary condition satisfied by the particle angular velocity at the liquid–solid interface. In the literature of magnetic liquids, one may specify a condition of the form (Rinaldi & Zahn 2002; Chaves *et al.* 2006; Chaves, Zahn & Rinaldi 2008)

$$\boldsymbol{\omega} = \boldsymbol{0}. \tag{2.13}$$

It may, however, be necessary to allow for a finite angular velocity at this boundary. Aero, Bulygin & Kuvshinskii (1965) allowed for rotation of the ferroparticles derived by the

balance of their overall angular velocity at the liquid–solid interface with the surface density of micro-moments:

$$\boldsymbol{\omega} = \hat{\boldsymbol{\lambda}}\hat{\boldsymbol{C}}\hat{\boldsymbol{n}}; \tag{2.14}$$

cf. Aero *et al.* (1965, equation (6.6)) where λ_{ij}, having units of length, is the inverse of the rotational friction tensor, and $\hat{\boldsymbol{n}}$ is normal at the solid–liquid interface so that the appearance of micro-moments at the surface is due to friction. We note that this boundary condition is analogous to the Navier slip condition of Newtonian fluid mechanics (Lauga, Brenner & Stone 2007), thus λ_{ij} is a rotational slip length. Its values will depend on surface roughness, liquid viscosity and particle size.

At the liquid–gas interface, the induction and magnetic field components are continuous:

$$[[\boldsymbol{b}\cdot\boldsymbol{n}]] = 0 \quad \text{and} \quad [[\boldsymbol{h}\cdot\boldsymbol{t}]] = 0. \tag{2.15a,b}$$

3. Reduction of the equations of motion

In the geometry displayed in figure 2 and in dimensional units, the liquid–gas interface lies at

$$z = \xi(x, t), \tag{3.1}$$

and the solid–liquid interface at $z = 0$. The fluid velocity $\boldsymbol{u}$, macroscopic particle angular velocity $\boldsymbol{\omega}$ and magnetization $\boldsymbol{m}$ obtain the component forms

$$(u(x, z, t), 0, w(x, z, t)), \quad (0, \omega(x, z, t), 0) \quad \text{and} \quad (m_1(x, z, t), 0, m_3(x, z, t)), \tag{3.2a–c}$$

respectively. The stress tensor (2.2) has the non-vanishing components

$$\sigma_{11} = -p + 2\eta u_x \quad \text{and} \quad \sigma_{13} = (\eta + \zeta)u_z + (\eta - \zeta)w_x - 2\zeta\omega, \tag{3.3a,b}$$

$$\sigma_{31} = (\eta - \zeta)u_z + (\eta + \zeta)w_x + 2\zeta\omega \quad \text{and} \quad \sigma_{33} = -p + 2\eta w_z, \tag{3.4a,b}$$

where a lower-case Latin subscript denotes differentiation with respect to the corresponding dimensional variable. For clarity and brevity, we did not explicitly include the Maxwell stress tensor components in these expressions because they give rise only to a body force whose effects are subdominant to those of the torque studied in the present paper (assuming weak fields and slow rotations); see the discussion in Kirkinis (2017, Appendix A). The couple stress tensor $\boldsymbol{C}$ has the non-zero components

$$C_{12} = C_{21} = \eta'\omega_x \quad \text{and} \quad C_{23} = C_{32} = \eta'\omega_z, \tag{3.5a,b}$$

and we assume that $\partial_j\omega_j = 0$ is also satisfied. Then the governing equations (2.1*a*,*b*) reduce to

$$\rho\left[u_t + uu_x + wu_z\right] = -p_x - 2\zeta\omega_z + (\zeta + \eta)(u_{xx} + u_{zz}) - \phi_x, \tag{3.6}$$

$$\rho\left[w_t + uw_x + ww_z\right] = -p_z + 2\zeta\omega_x + (\zeta + \eta)(w_{xx} + w_{zz}) - \phi_z, \tag{3.7}$$

$$I\left[\omega_t + u\omega_x + w\omega_z\right] = 2\zeta(u_z - w_x - 2\omega) + \eta'(\omega_{xx} + \omega_{zz}) + N, \tag{3.8}$$

where N is an applied magnetic torque, and the potential ϕ represents fields acting on the droplet, such as gravity and intermolecular forces. For the present analysis, we will

consider that ϕ represents the gravitational field acting on a droplet placed on an inclined substrate at angle ψ to the horizontal x-axis, leading to

$$\phi = \rho g(x \sin\psi + z\cos\psi). \tag{3.9}$$

The boundary conditions (2.12*a*,*b*) and (2.14) become

$$u = 0, \quad w = 0 \quad \text{and} \quad \omega = \lambda\omega_z, \quad \text{at } z = 0, \tag{3.10a–c}$$

respectively, which will be employed in our quasi-static analysis.

The tangent and normal vectors to the interface are, in Cartesian coordinates,

$$\boldsymbol{t} = (1, 0, \xi_x)/\sqrt{1+\xi_x^2} \quad \text{and} \quad \boldsymbol{n} = (-\xi_x, 0, 1)/\sqrt{1+\xi_x^2}, \tag{3.11a,b}$$

respectively. Thus at the liquid–gas interface $z = \xi(x, t)$, the boundary conditions (2.10*a*,*b*) read

$$\sigma_{13} - \xi_x^2\sigma_{31} + \xi_x(\sigma_{33} - \sigma_{11}) = 0 \quad \text{and} \quad \sigma_{33} + \xi_x^2\sigma_{11} - \xi_x(\sigma_{13} + \sigma_{31}) = \frac{\gamma\xi_{xx}}{\sqrt{1+\xi_x^2}}, \tag{3.12a,b}$$

where in (2.10*a*,*b*), we employed the expression for the curvature

$$2\mathcal{K} = \frac{\xi_{xx}}{(\sqrt{1+\xi_x^2})^3}. \tag{3.13}$$

Equation (2.11) becomes

$$\omega_z - \xi_x\omega_x = 0. \tag{3.14}$$

To the above, one may add the kinematic condition

$$w = \xi_t + u\xi_x \tag{3.15}$$

at the liquid–gas interface $z = \xi(x, t)$, which constitutes the starting point in deriving the sought-after evolution equation.

The problem of determining the motion of a droplet reduces to solving an evolution equation for the liquid–gas interface $z = \xi(x, t)$ with boundary conditions

$$\xi(c_a(t), t) = \xi(c_r(t), t) = 0, \quad \int_{c_r(t)}^{c_a(t)} \xi(x, t)\,\mathrm{d}x = V_0, \tag{3.16a,b}$$

where

$$c_a(t) \quad \text{and} \quad \theta_a(t), \quad c_r(t) \quad \text{and} \quad \theta_r(t) \tag{3.17a,b}$$

are the x-locations of the contact line and dynamic contact angles at the right and the left contact lines of the droplet, respectively (cf. figure 2). Following Smith (1995), we adopt the mobility law

$$\frac{\mathrm{d}c_a}{\mathrm{d}t} = \begin{cases} (\theta_a - \bar\theta_A)^m, & \theta_a > \bar\theta_A, \\ 0, & \bar\theta_R \leqslant \theta_a \leqslant \bar\theta_A, \\ -(\bar\theta_R - \theta_a)^m, & \theta_a < \bar\theta_R, \end{cases} \quad \text{and} \quad \frac{\mathrm{d}c_r}{\mathrm{d}t} = \begin{cases} -(\theta_r - \bar\theta_A)^m, & \theta_r > \bar\theta_A, \\ 0, & \bar\theta_R \leqslant \theta_r \leqslant \bar\theta_A, \\ (\bar\theta_R - \theta_r)^m, & \theta_r < \bar\theta_R, \end{cases} \tag{3.18a,b}$$

where $\theta_a(t) = -\xi_x(c_a(t))$ and $\theta_r(t) = \xi_x(c_r(t))$ (cf. figure 2), and

$$\bar\theta_A \quad \text{and} \quad \bar\theta_R \tag{3.19a,b}$$

are the advancing and receding static contact angles, respectively (cf. upper right corner of figure 2).

3.1. *Scalings for the lubrication approximation*

In this approximation, the Navier–Stokes equations (3.6) and (3.7), and internal angular momentum equation (3.8), are scaled with respect to small initial contact angle, characteristic droplet radius and droplet volume

$$\theta_0, \quad a_0 \quad \text{and} \quad V_0, \tag{3.20a–c}$$

respectively. This introduces slow longitudinal and slow temporal variables

$$X = \frac{x}{a_0}, \quad Z = \frac{z}{a_0\theta_0}, \quad T = \frac{k\theta_0^m}{a_0}\,t, \tag{3.21a–c}$$

where a_0 and θ_0 are characteristic scales for the liquid droplet spreading radius and initial contact angle, respectively, and the partial derivatives $\partial/\partial X$ and $\partial/\partial Z$ are now quantities of unit order (Ehrhard & Davis 1991; Oron *et al.* 1997; Davis 2002). The dimensionless velocity, particle angular velocity, pressure and liquid–gas interface location become, respectively,

$$U = \frac{u}{k\theta_0^m}, \quad W = \frac{w}{k\theta_0^{1+m}}, \quad \Omega = \frac{a_0\omega}{k\theta_0^{m-1}}, \quad P = \frac{a_0 p}{(\eta+\zeta)k\theta_0^{m-2}}, \quad \Xi = \frac{\xi}{a_0\theta_0}. \tag{3.22a–e}$$

We define the dimensionless Reynolds numbers, scaled capillary number and rotational slip coefficient (cf. (3.10*a–c*))

$$Re = \frac{\rho a_0 k\theta_0^{m+1}}{\eta+\zeta}, \quad Re' = \frac{Ia_0 k\theta_0^{m+1}}{\eta'}, \quad \bar{C} = \frac{(\eta+\zeta)k\theta_0^{m-3}}{\gamma}, \quad \Lambda = \frac{\lambda}{a_0\theta_0}, \tag{3.23a–d}$$

and dimensionless potential and torque

$$\Phi = \frac{\epsilon\xi_0\phi}{(\eta+\zeta)U_0}, \quad \bar{\mathcal{N}} = \frac{Na_0^3}{\eta' k\theta_0^{m-3}}. \tag{3.24a,b}$$

Finally, we define subsidiary dimensionless parameters α, β and κ:

$$\alpha = \frac{\zeta}{\eta+\zeta}, \quad \beta = 2\,\frac{\zeta a_0^2\theta_0^2}{\eta'}, \quad \kappa^2 \equiv 2\beta(1-\alpha) = \frac{4\eta\zeta a_0^2\theta_0^2}{\eta'(\eta+\zeta)}. \tag{3.25a–c}$$

Parameter α is important as it regulates the shear stress at the liquid–gas interface generated by the collective rotation of the rotating nanoparticles which gives rise to the effect discussed in this paper.

When the potential ϕ is due to a gravitational field as in (3.9), its dimensionless counterpart reads,

$$\Phi = \bar{G}\left(X\,\frac{\sin\psi}{\theta_0} + Z\cos\psi\right), \quad \bar{G} = \frac{\rho g a_0^2}{(\eta+\zeta)k\theta_0^{m-3}}. \tag{3.26a,b}$$

We note that although the above dimensionless groups are based on a small (initial) contact angle θ_0, they can be identified with the standard lubrication approximation groups

developed by Oron *et al.* (1997) by performing the substitution

$$\theta_0 \to \epsilon, \quad a_0\theta_0 \to \xi_0, \quad k\theta_0^m \to U_0. \tag{3.27a–c}$$

With the above notation, and by setting $\theta_0 = \epsilon$ (3.6)–(3.8) obtain the following dimensionless form:

$$\epsilon\, Re\,[U_T + UU_X + WU_Z] = -P_X - 2\alpha\Omega_Z + (\epsilon^2 U_{XX} + U_{ZZ}) - \Phi_X, \tag{3.28}$$

$$\epsilon^2\, Re\,[W_T + UW_X + WW_Z] = -\frac{1}{\epsilon}P_Z + 2\epsilon\alpha\Omega_X + \epsilon(\epsilon^2 W_{XX} + W_{ZZ}) - \frac{1}{\epsilon}\Phi_Z, \tag{3.29}$$

$$\epsilon\, Re'\,[\Omega_T + U\Omega_X + W\Omega_Z] = \beta(U_Z - \epsilon^2 W_X - 2\Omega) + \epsilon^2\Omega_{XX} + \Omega_{ZZ} + \bar{\mathcal{N}}. \tag{3.30}$$

The boundary conditions (3.10*a–c*), (3.12*a*,*b*), (3.14), become respectively

$$U = 0, \quad W = 0, \quad \Omega = \Lambda\Omega_Z, \quad \text{at } Z = 0, \tag{3.31a–c}$$

and

$$U_Z - 2\alpha\Omega + O(\epsilon) = 0, \quad -P = \bar{C}^{-1}\Xi_{XX} + O(\epsilon), \quad \Omega_Z + O(\epsilon) = 0, \quad \text{at } Z = \Xi(X,T). \tag{3.32a–c}$$

The kinematic condition (3.15) becomes $W = \Xi_T + U\Xi_X$, and leads to the following evolution equation for the profile Ξ:

$$\Xi_T + \left[\int_0^{\Xi} U\,\mathrm{d}Z\right]_X = 0. \tag{3.33}$$

This is obtained in the standard way (Oron *et al.* 1997) by integrating the incompressibility condition $U_X + W_Z = 0$ from $Z = 0$ to $Z = \Xi(X,T)$, using the second equation of (3.31*a–c*) and integration by parts.

We proceed by expanding all fields in a regular perturbation expansion with respect to the small parameter ϵ: $(U, W, P, \Omega) = (U^0, W^0, P^0, \Omega^0) + \epsilon(U^1, W^1, P^1, \Omega^1) + O(\epsilon^2)$. To leading order (which corresponds to the lubrication approximation) and dropping superscripts denoting order in ϵ, scaled equations (3.28)–(3.30) simplify to

$$-P_X - 2\alpha\Omega_Z + U_{ZZ} - \Phi_X = 0, \quad -P_Z - \Phi_Z = 0, \quad \beta(U_Z - 2\Omega) + \Omega_{ZZ} + \bar{\mathcal{N}} = 0. \tag{3.34a–c}$$

To the above, one should add the corresponding expressions for the magnetization equation and magnetic fields, which are identical to Kirkinis (2017, (4.20*a*,*b*) and (4.21*a*,*b*)) and need not be repeated here,

$$U_Z - 2\alpha\Omega = 0, \quad -P = \bar{C}^{-1}\Xi_{XX}, \quad \Omega_Z = 0, \quad \text{at } Z = \Xi(X,T), \tag{3.35a–c}$$

and the boundary conditions at the liquid–solid interface remain the same as (3.31*a–c*) with the understanding that they now refer to the leading-order approximation.

Integration of the second equation of (3.34*a–c*) and application of the normal stress boundary condition (second equation of (3.35*a–c*)) leads to the reduced pressure $\bar{P}(X,T) \equiv P + \Phi = \Phi|_{Z=\Xi} - \bar{C}^{-1}\Xi_{XX}$. Thus when Φ is associated with gravity, the

pressure reads

$$\bar{P}(X,T) = \bar{G}\left(X\frac{\sin\psi}{\theta_0} + \Xi\cos\psi\right) - \bar{C}^{-1}\Xi_{XX}. \tag{3.36}$$

Thus the problem of determining the motion of a droplet reduces to solving the evolution equation (3.33) with boundary conditions

$$\Xi(c_a(t)/a_0) = \Xi(c_r(t)/a_0) = 0, \quad \int_{c_r(t)/a_0}^{c_a(t)/a_0} \Xi(X)\,\mathrm{d}X = 1, \tag{3.37a,b}$$

and the mobility law (3.18*a*,*b*) (cf. figure 2), along with suitable initial conditions.

In the limit $\omega\tau_B \ll 1$ (the Brownian relaxation time τ_B was defined in (2.7)), the magnetic torque appearing in (3.34*a*–*c*) can be considered as a constant; cf. Zahn & Greer (1995) and Kirkinis (2017). Then (3.34*a*–*c*) yield closed form expressions for the fields U, W and Ω (whose exact forms appear in Appendix A). Thus the flux function in (3.33) becomes

$$\begin{aligned}\int_0^{\Xi} U\,\mathrm{d}Z = {}& \frac{\alpha}{6\kappa^3(\alpha-1)\beta(\cosh\kappa\Xi + \Lambda\kappa\sinh\kappa\Xi)}\\ &\times\left\{\left(\left(-6\beta\kappa\left(\Xi\sinh(\kappa\Xi)\kappa - 2\cosh(\kappa\Xi) + 2\right)\alpha + 2\Xi^3\sinh(\kappa\Xi)\beta\kappa^4\right)\Lambda\right.\right.\\ &- 6\beta\left(\Xi^2\sinh(\kappa\Xi)\kappa^2 - \Xi\cosh(\kappa\Xi)\kappa + 2\kappa\Xi - \sinh(\kappa\Xi)\right)\alpha\\ &+ 2\Xi^3\cosh(\kappa\Xi)\beta\kappa^3\Big)\bar{P}_X + \Big(-3\Xi^2\alpha\kappa^4\sinh(\kappa\Xi)\Lambda\\ &\left.\left. - 3\alpha\kappa\left(\Xi^2\cosh(\kappa\Xi)\kappa^2 - 2\Xi\sinh(\kappa\Xi)\kappa + 2\cosh(\kappa\Xi) - 2\right)\right)\bar{\mathcal{N}}\right\},\end{aligned} \tag{3.38}$$

where the parameters α, β and κ were defined in (3.25*a*–*c*). This equation should be contrasted to the flux function $\int_0^{\Xi} U\,\mathrm{d}Z = -\frac{1}{3}\bar{P}_X\Xi^3$ obtained in the absence of the rotational degrees of freedom (Oron *et al.* 1997; Davis 2002). Setting $\Lambda = 0$, (3.38) reduces to (4.24) of Kirkinis (2017).

It is difficult to extract any physical meaning directly from the flux function (3.38). We thus seek an asymptotic limit $\Xi \to 0$ to obtain

$$\begin{aligned}\int_0^{\Xi} U\,\mathrm{d}Z = {}& \left(\bar{\mathcal{N}}\Lambda\alpha - \frac{1}{3}\bar{P}_X\right)\Xi^3 + 2\alpha\left(\beta\bar{\mathcal{N}}(\alpha-1)\Lambda^2 - \frac{1}{4}\bar{P}_X\beta\Lambda + \frac{1}{8}\bar{\mathcal{N}}\right)\Xi^4\\ &+ \left(4\beta\bar{\mathcal{N}}(\alpha-1)^2\Lambda^3 - \bar{P}_X\beta(\alpha-1)\Lambda^2 + \frac{7\bar{\mathcal{N}}(\alpha-1)\Lambda}{6} - \frac{\bar{P}_X}{10}\right)\beta\alpha\Xi^5\\ &+ O(\Xi^6),\end{aligned} \tag{3.39}$$

where the effects of magnetic torque $\bar{\mathcal{N}}$, pressure gradient $\bar{P}_X$ and rotational slip length Λ become evident.

In the ensuing sections, we will be interested in two limits of the evolution equation (3.33) with flux function (3.39). First is the case of non-zero rotational slip Λ and torque

$\bar{\mathcal{N}}$, where the evolution equation, to leading order in Ξ, obtains the form

$$\Xi_T + \alpha\Lambda\bar{\mathcal{N}}\Xi^2\Xi_X - \tfrac{1}{3}(\Xi^3\bar{P}_X)_X \sim 0. \tag{3.40}$$

In the second case, we set $\Lambda \equiv 0$ and the evolution equation reduces to a known form (cf. Kirkinis 2017, equation (5.1))

$$\Xi_T + \alpha\bar{\mathcal{N}}\Xi^3\Xi_X - \tfrac{1}{3}(\Xi^3\bar{P}_X)_X \sim 0, \tag{3.41}$$

whose nonlinear term multiplying the torque has been shown to give rise to nonlinear interfacial capillary wave propagation in the context of stabilization mechanisms of thin liquid films (Kirkinis & Davis 2015).

The form of the two nonlinear evolution equations (3.40) and (3.41) can be justified in an alternative way. Consider κ to be the small parameter $\kappa \sim \xi_0 \equiv a_0\theta_0$ (see the third equation of (3.25*a–c*)), and expand the flux function (3.38) with respect to this parameter. The result is

$$\int_0^{\Xi} U\,\mathrm{d}Z = \frac{\Xi^3(\alpha\,(4\Lambda + \Xi)\,\bar{\mathcal{N}} - \frac{4}{3}\bar{P}_X)}{4} + O(\kappa^2). \tag{3.42}$$

Thus (3.40) is obtained when $\xi \ll \lambda$ and $\xi \ll (\eta'/\eta)(p_x/N)$, achieved for sufficiently small droplets, and (3.41) is obtained when $\Lambda \equiv 0$.

4. Droplet migration on a horizontal substrate

4.1. *Small capillary number expansion*

In the following discussion, it will be convenient to introduce the dimensionless Bond number and torque as

$$G \equiv \bar{G}\bar{C} = \frac{\rho g a_0^2}{\gamma} \quad \text{and} \quad \mathcal{N} \equiv \bar{C}\bar{\mathcal{N}} = \frac{(\eta+\zeta)a_0^3 N}{\eta'\gamma}. \tag{4.1a,b}$$

We will be interested in the limit of small capillary number $\bar{C}$. We rewrite equations (3.40) and (3.41) in the form

$$\bar{C}\Xi_T + \alpha\Lambda\mathcal{N}\Xi^2\Xi_X - \tfrac{1}{3}(\Xi^3\bar{C}\bar{P}_X)_X \sim 0 \tag{4.2}$$

and

$$\bar{C}\Xi_T + \alpha\mathcal{N}\Xi^3\Xi_X - \tfrac{1}{3}(\Xi^3\bar{C}\bar{P}_X)_X \sim 0, \tag{4.3}$$

respectively, where

$$\bar{C}\bar{P}_X = G\left(\frac{\sin\psi}{\theta_0} + \Xi_X\cos\psi\right) - \Xi_{XXX}. \tag{4.4}$$

As discussed by Ehrhard & Davis (1991, § 5), in taking the limit $\bar{C} \to 0$, one considers the 'outer' asymptotic expansion for the liquid–gas interface profile Ξ in powers of the capillary number and neglects an initial layer.

Studying (4.2) and (4.3) in the limit $\bar{C} \to 0$ will, from now on, be the exclusive content of the analysis to follow.

4.2. *Rotating nanoparticles at the substrate* $\Lambda \neq 0, \mathcal{N} \neq 0$

In this case, the quasi-static equation (4.2) in the limit of small capillary number and flat substrate ($\psi = 0$) becomes

$$\Xi_{XXX} - G\Xi_X + 3\alpha\Lambda\mathcal{N} = 0, \tag{4.5}$$

where the Bond number G and torque $\mathcal{N}$ were defined in (4.1*a*,*b*). The liquid–gas interface profile obtains the form

$$\Xi(X,T) = C_1\,\mathrm{e}^{GX} + C_2\,\mathrm{e}^{-GX} + C_3 + \frac{3\alpha\Lambda\mathcal{N}X}{G}, \tag{4.6}$$

where the C_i are constants of integration. Employing the boundary conditions (3.37*a*,*b*) and reverting to a frame of reference whose origin lies at the centre of the base of the droplet (see S A.1), we obtain the profile

$$\Xi(X,T) = \frac{\sqrt{G}}{2}\,\frac{\cosh X\sqrt{G} - \cosh A\sqrt{G}}{\sinh A\sqrt{G} - A\sqrt{G}\cosh A\sqrt{G}} + 3\alpha\Lambda\mathcal{N}\,\frac{X\sinh A\sqrt{G} - A\sinh X\sqrt{G}}{G\sinh A\sqrt{G}}, \tag{4.7}$$

where

$$A(t) = \frac{c_a(t) - c_r(t)}{2a_0} \tag{4.8}$$

is the dimensionless droplet radius. When $\Lambda \equiv 0$, (4.7) recovers the liquid–gas profile of Ehrhard & Davis (1991, equation (6.1*p*)) for isothermal spreading of a droplet, in the presence of a vertical temperature gradient.

The dynamic contact angle $\theta_a(t)$ on the right of the droplet (cf. figure 2) reads

$$\theta_a(t) = \frac{G}{2}\,\frac{-\sinh A\sqrt{G}}{\sinh A\sqrt{G} - A\sqrt{G}\cosh A\sqrt{G}} + 3\alpha\Lambda\mathcal{N}\,\frac{A\sqrt{G}\cosh A\sqrt{G} - \sinh A\sqrt{G}}{G\sinh A\sqrt{G}}, \tag{4.9}$$

and its counterpart at the left of the droplet reads $\theta_r(t,\mathcal{N}) = \theta_a(t,-\mathcal{N})$.

Although our approach is not perturbative, we can still employ the general treatment of Appendix B to form the droplet migration velocity

$$U_{CL} = \left(3\alpha\Lambda\mathcal{N}\,\frac{A\sqrt{G}\cosh A\sqrt{G} - \sinh A\sqrt{G}}{G\sinh A\sqrt{G}} - \frac{\bar{\theta}_A - \bar{\theta}_R}{2}\right)^m. \tag{4.10}$$

In figure 3, we show that during migration, the droplet radius reaches a fixed point ($a(t)/a_0 \sim 1.14706$) irrespective of the initial conditions. At the same time, the velocity of the midpoint of the droplet, $\mathrm{d}(\bar{c}/a_0)/\mathrm{d}t$, also reaches a fixed point, that is, the fixed value U_{CL}, denoting the theoretical value of the dimensionless migration velocity that we derive in (4.10) evaluated at the fixed point attained asymptotically by the radius $a(t)/a_0 \sim 1.14706$ in figure 3(*a*). The results are obtained by solving the piecewise mobility law (3.18*a*,*b*) with contact angles taken from (4.9). Thus figure 3 shows excellent agreement between our theoretical calculations and numerical simulations.

Figure 4 displays the droplet migration on a solid substrate with velocity U_{CL} (cf. (4.10)) whose profiles are calculated from (4.7) by incorporating the contact angles (4.9) into the mobility law (3.18*a*,*b*). Thus the magnetic-torque-induced deformation of the droplet leads to a left–right asymmetry of the contact angles that overcomes hysteresis effects (at

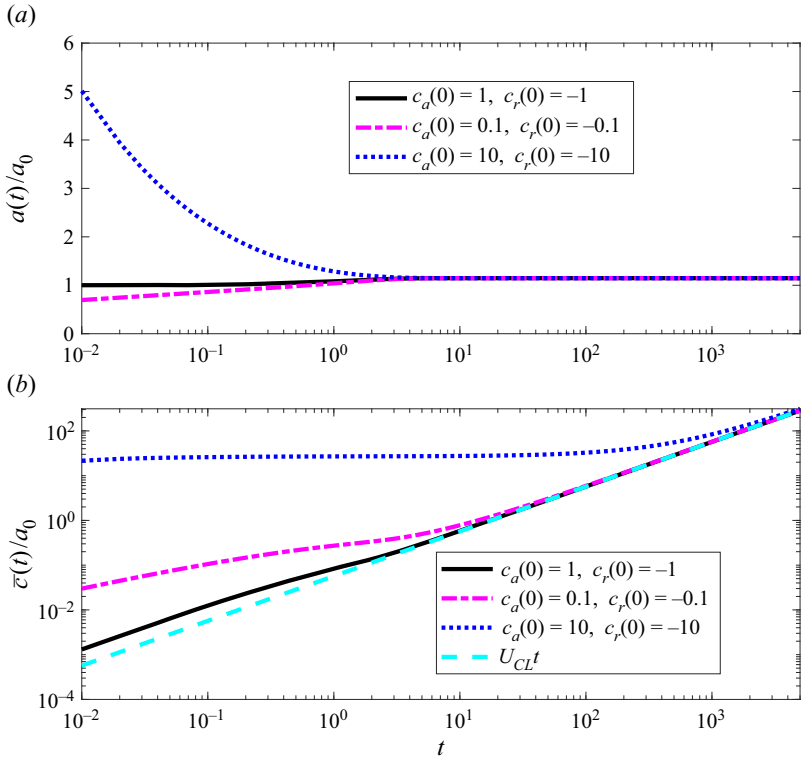

Figure 3. (*a*) Time evolution of dimensionless droplet radius $a(t)/a_0$ by solving (3.18*a*,*b*) with contact angles taken from (4.9) for the case of finite particle angular velocity at the liquid–solid interface. Here, $G = 0.1$, $3\alpha\Lambda\mathcal{N} = 1$, $m = 3$ and $(\bar{\theta}_A - \bar{\theta}_R)/\theta_0 = 0.1$. Independent of initial data, the radius converges to a fixed width $a(t)/a_0 = 1.14706$. (*b*) Time evolution of dimensionless droplet midpoint $\bar{c}(t)/a_0$. Independent of initial data, the midpoint acquires a slope proportional to U_{CL}, the latter denoting the theoretical value of the dimensionless migration velocity that we derive in (4.10) evaluated at the fixed point attained asymptotically by the radius $a(t)/a_0 \sim 1.14706$ in (*a*).

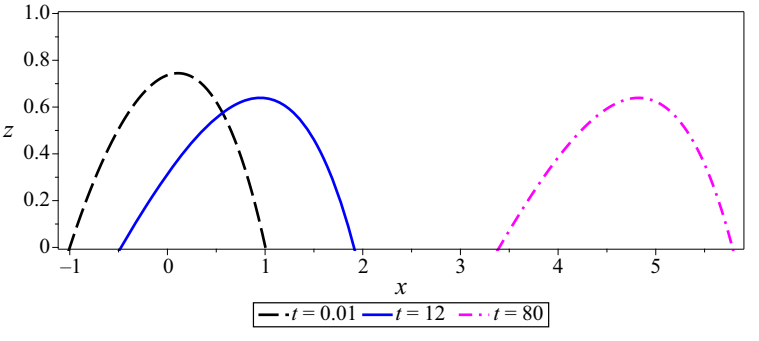

Figure 4. Magnetic droplet profiles calculated from (4.7) migrate on a solid substrate with velocity U_{CL} (cf. (4.10)). The effect is due to finite particle angular velocity at the liquid–solid substrate $3\alpha\Lambda\mathcal{N} = 4$ (see boundary condition (3.31*a–c*)) coupled with the magnetic torque. The combined effects of particle rotation at both the liquid–gas and liquid–solid interfaces leads to a left–right asymmetry in the contact angles, migration and a commensurate deformation. The profiles were generated by solving (3.18*a*,*b*) with dynamical contact angles $\theta_a(t)$ and $\theta_r(t)$ from (4.9), and static advancing and receding contact angles $\theta_A = 1.2$ and $\theta_R = 1.1$ (both scaled by the initial contact angle θ_0).

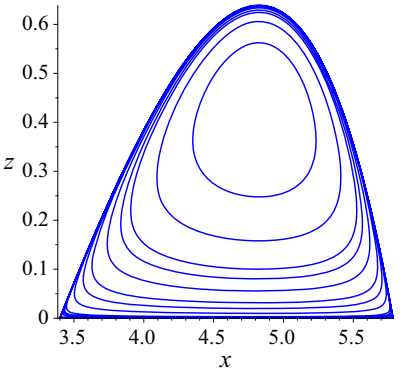

Figure 5. Droplet migration with $3\alpha\Lambda\mathcal{N} = 4$ at time $t = 80$, as displayed in figure 4. The synergy between the magnetic torque and the solid-surface tank-treading embodied in the 'forcing' term $3\alpha\Lambda\mathcal{N}$ of (4.5) deforms the droplet and its streamlines, breaks the left–right symmetry of the contact angles, and leads to migration with velocity U (cf. (4.10)).

a sufficiently strong magnitude of the torque), as this is displayed in (4.10), and leads to droplet migration.

Figure 5 displays the streamlines at the final time of figure 4. The streamlines are closed, and the liquid performs a clockwise rotation. To obtain this figure, the streamfunction

$$\Psi(X, Z) = \int_0^Z U(X, Z)\,\mathrm{d}Z \tag{4.11}$$

was substituted into the profile (4.7) by expanding to first order in H to match the asymptotics leading to (4.5). For this problem, because $\bar{C}\bar{P}_X = 3\Lambda\alpha\mathcal{N}$, we can replace the pressure gradient in the expression for U and thus Ψ with the constant $3\alpha\Lambda\mathcal{N}$.

We note that the above results can be expressed concisely with respect to the Langevin function

$$\mathcal{L}(x) = \coth x - \frac{1}{x}. \tag{4.12}$$

Thus

$$\theta_a(t) = \frac{\sqrt{G}}{2A}\,\frac{1}{\mathcal{L}(A\sqrt{G})} + 3\alpha\Lambda\mathcal{N}\,\frac{A}{\sqrt{G}}\,\mathcal{L}(A\sqrt{G}) \tag{4.13}$$

and

$$U_{CL} = \left(3\alpha\Lambda\mathcal{N}\,\frac{A}{\sqrt{G}}\,\mathcal{L}(A\sqrt{G}) - \frac{\bar{\theta}_A - \bar{\theta}_R}{2}\right)^m. \tag{4.14}$$

The required torque strength that would give rise to droplet migration is

$$\mathcal{N} > \frac{\sqrt{G}}{3\alpha\Lambda A\,\mathcal{L}(A\sqrt{G})}\,\frac{\bar{\theta}_A - \bar{\theta}_R}{2} \quad \text{or} \quad N > \frac{\eta'\gamma\sqrt{\rho g/\gamma}\,\Delta\theta}{6\zeta\lambda a_0\,\mathcal{L}\left(a_0\sqrt{\rho g/\gamma}\right)}, \tag{4.15}$$

where $\Delta\theta = \bar{\theta}_A - \bar{\theta}_R$. The above expressions are very useful as they provide estimates of the observables for all ranges of capillary lengths. For instance, in the limit of small droplets ($A\sqrt{G} \ll 1$, or equivalently, $a \ll a_{cap}$; see below), resorting to the series

expansion $\mathcal{L}(x) \sim x/3 - x^3/45$ of the Langevin function, we obtain results corresponding to (4.13)–(4.15) that are independent of gravity:

$$\theta_a(t) \sim \frac{3}{2A^2} + \alpha \Lambda \mathcal{N} A^2, \quad U_{CL} \sim \left(\alpha \Lambda \mathcal{N} A^2 - \frac{\bar{\theta}_A - \bar{\theta}_R}{2}\right)^m, \quad \mathcal{N} > \frac{\bar{\theta}_A - \bar{\theta}_R}{2\alpha \Lambda A^2}. \tag{4.16a–c}$$

The leading-order expression in θ_a is the same as the corresponding leading-order terms of the spreading (Ehrhard & Davis 1991, equation (7.3p)) and migration (Smith 1995, equation (15a)) results. The argument of the Langevin function $A\sqrt{G}$ is related to the capillary length a_{cap} by

$$A(t)\sqrt{G} = \frac{a(t)}{a_{cap}}, \quad \text{where } a_{cap} = \sqrt{\frac{\gamma}{\rho g}}, \tag{4.17}$$

recalling that the dimensional and dimensionless droplet radii are defined by $a(t) = (c_a(t) - c_r(t))/2$ and $A(t) = a(t)/a_0$, respectively. Thus with respect to dimensional parameters, the migration velocity reads

$$u_{CL} = k\left[\frac{3\zeta \lambda N a a_{cap}}{\eta' \gamma}\mathcal{L}\left(\frac{a}{a_{cap}}\right) - \frac{\bar{\theta}_A - \bar{\theta}_R}{2}\right]^m \sim k\left[\frac{3\zeta \lambda N a^2}{\eta' \gamma} - \frac{\bar{\theta}_A - \bar{\theta}_R}{2}\right]^m. \tag{4.18}$$

The required torque strength (4.15) that gives rise to migration is

$$N > \frac{\eta' \gamma (\bar{\theta}_A - \bar{\theta}_R)}{6\zeta a a_{cap} \lambda \mathcal{L}(a/a_{cap})} \sim \frac{\eta' \gamma (\bar{\theta}_A - \bar{\theta}_R)}{2\zeta \lambda a^2}, \tag{4.19}$$

and the approximation in (4.18) and (4.19) is applied in the limit $a \ll a_{cap}$.

We see that the above results are a direct consequence of the presence of a magnetic torque N, the antisymmetric stress ($\zeta \neq 0$) and the couple stress ($\eta' \neq 0$) of the constitutive laws (2.2) and (2.4), respectively.

For certain applications, for instance those promoting active surfaces (cf. figure 1 and Torres-Díaz & Rinaldi 2014), one will be interested in estimating the liquid velocity at the peak of the interface $z = \xi(x, t)$. This is given by the tangential velocity $u_t(x, h) = \boldsymbol{u} \cdot \hat{\boldsymbol{t}}$, that is, the component of the interfacial velocity in the direction of the tangential vector $\hat{\boldsymbol{t}}$ defined below (3.10a–c). Thus

$$U_t = \frac{1}{2}\alpha \Lambda \bar{\mathcal{N}} \Xi^2 + O(\Xi^4), \quad \text{or} \quad u_t = \frac{\zeta \lambda}{2(\eta + \zeta)\eta'} N\xi^2 + O(\xi^4) \tag{4.20}$$

in the limit of small thickness.

In figure 6, we display droplet snapshots taken at various regimes formed in the $G, \mathcal{N}$ plane for a given initial droplet configuration with spreading radius $A = 2(3/(2\bar{\theta}_A))^{1/2}$, in a manner similar to the numerical simulations of Smith (1995, figure 2). Here, however, our results are exact, thus we do not resort to numerical analysis or perturbation expansions as was the case in the non-isothermal migration of droplets in Smith (1995). The interpretation of the various regimes is given in figure 6(b). Pure migration (without spreading or receding contact angles) takes place at the central vertical line $\theta_a(t) - \bar{\theta}_A = -\theta_r(t) + \bar{\theta}_R$, for all marked torque values, from its intersection with the $\theta_a = \bar{\theta}_A$ and $\theta_r(t) = \bar{\theta}_R$ curves to its intersection with the $\theta_r(t) = 0$ curve.

In figure 7, we display droplet snapshots taken at various regimes formed in the $A, \mathcal{N}$ plane for the value $G = 1$ of the Bond number. The interpretation of the various regimes is

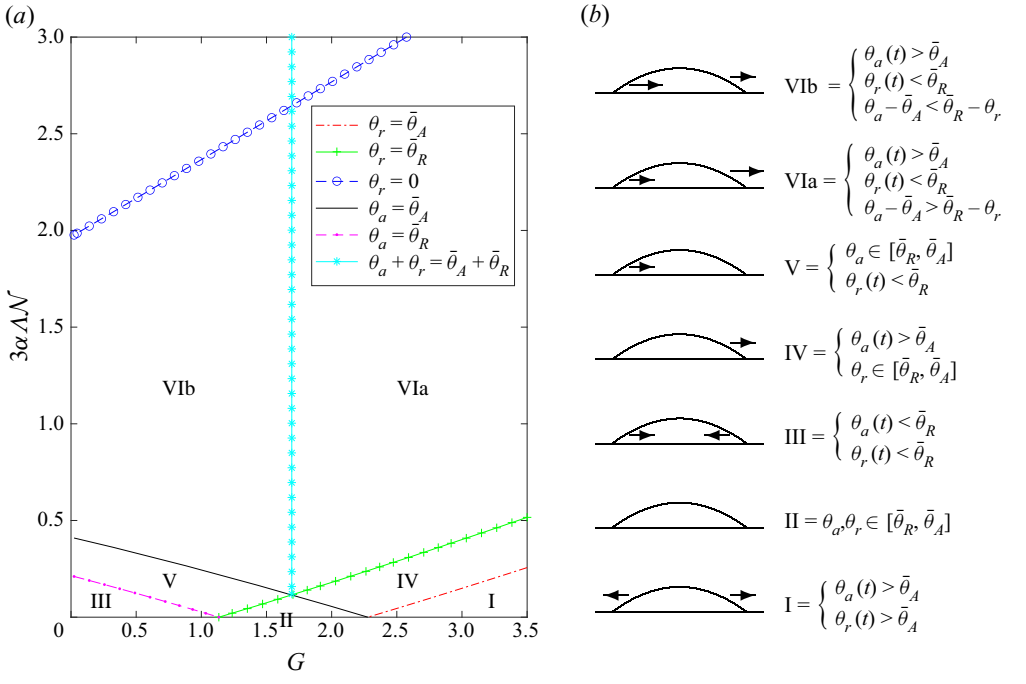

Figure 6. Parameter plot for Bond number $G = \rho g a_0^2/\gamma$ versus dimensionless torque $3\alpha\Lambda\mathcal{N} = 3\lambda\zeta a_0^2 N/(\eta'\gamma)$ (cf. (4.1*a*,*b*) and Smith 1995, figure 2) for the evolution of the droplet with static advancing and receding contact angles $\bar{\theta}_A = 1.2$ and $\bar{\theta}_R = 1.1$ (scaled by θ_0), away from an initial state of dimensionless droplet radius $A = 4.141$, by employing (4.9) and its receding counterpart. The seven allowed regions describe: I, two-sided spreading; II, pinned (immobile) droplet; III, receding droplet; IV, pinned left, spreading right contact line; V, pinned right, receding left contact line; VIa, droplet migrates and spreads; VIb droplet migrates and recedes. The delineations correspond to $\theta_r(t) = \bar{\theta}_A$, $\theta_r(t) = \bar{\theta}_R$, $\theta_r(t) = 0$, $\theta_a(t) = \bar{\theta}_A$, $\theta_a(t) = \bar{\theta}_R$, $\theta_a(t) - \bar{\theta}_A = -\theta_r(t) + \bar{\theta}_R$. The upper left corner region of the plot (above the line $\theta_r = 0$) corresponds to unphysical behaviour.

given in figure 7(*b*). Pure migration (without spreading or receding contact angles) takes place at the central vertical line $\theta_a(t) - \bar{\theta}_A = -\theta_r(t) + \bar{\theta}_R$, for all marked torque values, from its intersection with the $\theta_a = \bar{\theta}_A$ and $\theta_r(t) = \bar{\theta}_R$ curves to its intersection with the $\theta_r(t) = 0$ curve.

4.3. *Immobile nanoparticles at the substrate: $\Lambda = 0, \mathcal{N} \neq 0$*

In this case, the particle angular velocity at the solid–liquid substrate vanishes ($\Omega = 0$ at $Z = 0$). The quasi-static equation (4.3) in the limit of small capillary number becomes

$$\Xi_{XXX} - G\Xi_X + \tfrac{3}{4}\alpha\mathcal{N}\Xi = 0, \tag{4.21}$$

where the Bond number G and torque $\mathcal{N}$ were defined in (4.1*a*,*b*). We consider the zero gravity case ($G = 0$) for simplicity, which would apply to very small droplets. Then the

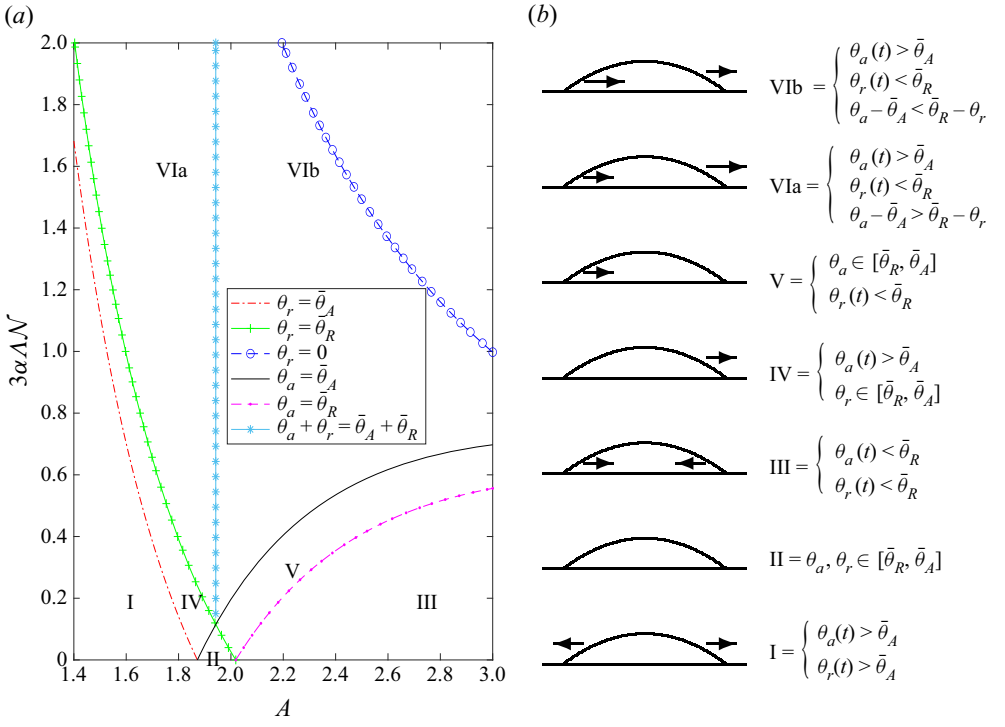

Figure 7. Parameter plot for dimensionless droplet radius $A = (c_a(t) - c_r(t))/2a_0$ versus dimensionless torque $3\alpha\Lambda\mathcal{N} = 3\lambda\zeta a_0^2 N/(\eta'\gamma)$ (cf. (4.1*a*,*b*)) for the evolution of the droplet with static advancing and receding contact angles $\bar{\theta}_A = 1.2$ and $\bar{\theta}_R = 1.1$ (scaled by θ_0), for Bond number $G = 1$, by employing (4.9) and its receding counterpart. The seven allowed regions describe: I, two-sided spreading; II, pinned (immobile) droplet; III, receding droplet; IV, pinned left, spreading right contact line; V, pinned right, receding left contact line; VIa, droplet migrates and spreads; VIb droplet migrates and recedes. The delineations correspond to $\theta_r(t) = \bar{\theta}_A$, $\theta_r(t) = \bar{\theta}_R$, $\theta_r(t) = 0$, $\theta_a(t) = \bar{\theta}_A$, $\theta_a(t) = \bar{\theta}_R$, $\theta_a(t) - \bar{\theta}_A = -\theta_r(t) + \bar{\theta}_R$. The upper right corner region of the plot (above the line $\theta_r = 0$) corresponds to unphysical behaviour.

liquid–gas profile obtained from (4.21) becomes

$$\Xi = c_1 \exp\left(-\left(\frac{3}{4}\alpha\mathcal{N}\right)^{1/3} X\right) + \exp\left(\left(\frac{3}{32}\alpha\mathcal{N}\right)^{1/3} X\right)\left[c_2 \cos\left(\frac{9\sqrt{3}}{32}\alpha\mathcal{N}\right)^{1/3} X + c_3 \sin\left(\frac{9\sqrt{3}}{32}\alpha\mathcal{N}\right)^{1/3} X\right], \tag{4.22}$$

where c_i are integration constants, and the exponents are determined from the cubic root of $-\frac{3}{4}\alpha\mathcal{N}$. Employing the boundary conditions (3.37*a*,*b*), the dynamic right and left contact angles become, respectively,

$$\theta_a(t) = \left(\tfrac{3}{4}\alpha\mathcal{N}\right)^{2/3} \frac{\exp\left(3A(\frac{3}{4}\alpha\mathcal{N})^{1/3}\right) - \sqrt{3}\sin - \cos}{-\left(\sqrt{3}\sin + \cos\right)\exp\left(2A(\frac{3}{4}\alpha\mathcal{N})^{1/3}\right) + \exp\left(3A(\frac{3}{4}\alpha\mathcal{N})^{1/3} + \sqrt{3}\sin - \cos\right)} \tag{4.23}$$

and

$$\theta_r(t) = \left(\tfrac{3}{4}\,\alpha\mathcal{N}\right)^{2/3} \exp\left(-A\left(\tfrac{3}{4}\,\alpha\mathcal{N}\right)^{1/3}\right) \times \frac{1 + \exp\left(3A(\tfrac{3}{4}\alpha\mathcal{N})^{1/3}\right)\left(\sqrt{3}\sin - \cos\right)}{-\left(\sqrt{3}\sin + \cos\right)\exp\left(2A(\tfrac{3}{4}\alpha\mathcal{N})^{1/3}\right) + \exp\left(3A(\tfrac{3}{4}\alpha\mathcal{N})^{1/3}\right) + \sqrt{3}\sin - \cos}, \tag{4.24}$$

where the argument of the trigonometric functions is $\sqrt{3}(\frac{3}{4}\alpha\mathcal{N})^{1/3}A$.

To calculate the migration velocity U_{CL} and required torque for this problem, one can easily form the expression

$$U_{CL} = \left[\frac{\theta_a(t) - \theta_r(t)}{2} - \frac{\bar{\theta}_A - \bar{\theta}_R}{2}\right]^m, \tag{4.25}$$

resorting to (4.23) and (4.24). Explicitly,

$$U_{CL} = \left[\tfrac{1}{2}\left(\tfrac{3}{4}\,\alpha\mathcal{N}\right)^{2/3} \frac{\sinh 2a(\tfrac{3}{4}\alpha\mathcal{N})^{1/3} - \sqrt{3}\cosh\times\sin + \sinh\times\cos}{\exp\left(2a(\tfrac{3}{4}\alpha\mathcal{N})^{1/3}\right) - \sqrt{3}\sinh\times\sin - \cosh\times\cos} - \frac{\bar{\theta}_A - \bar{\theta}_R}{2}\right]^m, \tag{4.26}$$

where the arguments of the trigonometric and hyperbolic functions are $\sqrt{3}(\frac{3}{4}\alpha\mathcal{N})^{1/3}A$ and $(\frac{3}{4}\alpha\mathcal{N})^{1/3}A$, respectively. In figure 8, we show that during migration, the droplet radius reaches a fixed point ($a(t)/a_0 \sim 1.14562$) irrespective of the initial conditions. At the same time, the velocity of the midpoint of the droplet $\mathrm{d}(\bar{c}/a_0)/\mathrm{d}t$ also reaches a fixed point, that is, the fixed value U_{CL} denoting the theoretical value of the dimensionless migration velocity that we derive in (4.26) evaluated at the fixed point attained asymptotically by the radius $a(t)/a_0 \sim 1.14562$ in figure 8(*a*). The results are obtained by solving the piecewise mobility law (3.18*a*,*b*) with contact angles taken from (4.23). Thus figure 8 shows excellent agreement between our theoretical calculations and numerical simulations.

Figure 9 displays the droplet migration on a solid substrate with velocity U_{CL} (cf. (4.26)) whose profiles are calculated from (4.22) by incorporating the contact angles (4.23) and (4.24) into the mobility law (3.18*a*,*b*). Thus the magnetic-torque-induced deformation of the droplet leads to a left–right asymmetry of the contact angles that overcomes hysteresis effects (at a sufficiently strong magnitude of the torque), as this is displayed in (4.26), and leads to droplet migration. Figure 10 displays the streamlines at the final time of figure 9.

It is instructive to derive the corresponding expressions in the limit $\mathcal{N} \to 0$:

$$\theta_a \sim \frac{3}{2A^2} + \frac{3A}{20}\,\alpha\mathcal{N}, \quad \theta_r \sim \frac{3}{2A^2} - \frac{3A}{20}\,\alpha\mathcal{N}, \tag{4.27a,b}$$

which form a special case of the general perturbative formulation developed in Appendix B. Thus the migration velocity becomes

$$U_{CL} \sim \left[\frac{3a}{20}\,\alpha\mathcal{N} - \frac{\bar{\theta}_A - \bar{\theta}_R}{2}\right]^m, \quad \text{or} \quad u_{CL} \sim k\left[\frac{3\zeta a_0^3 N}{20\eta'\gamma} - \frac{\bar{\theta}_A - \bar{\theta}_R}{2}\right]^m, \tag{4.28}$$

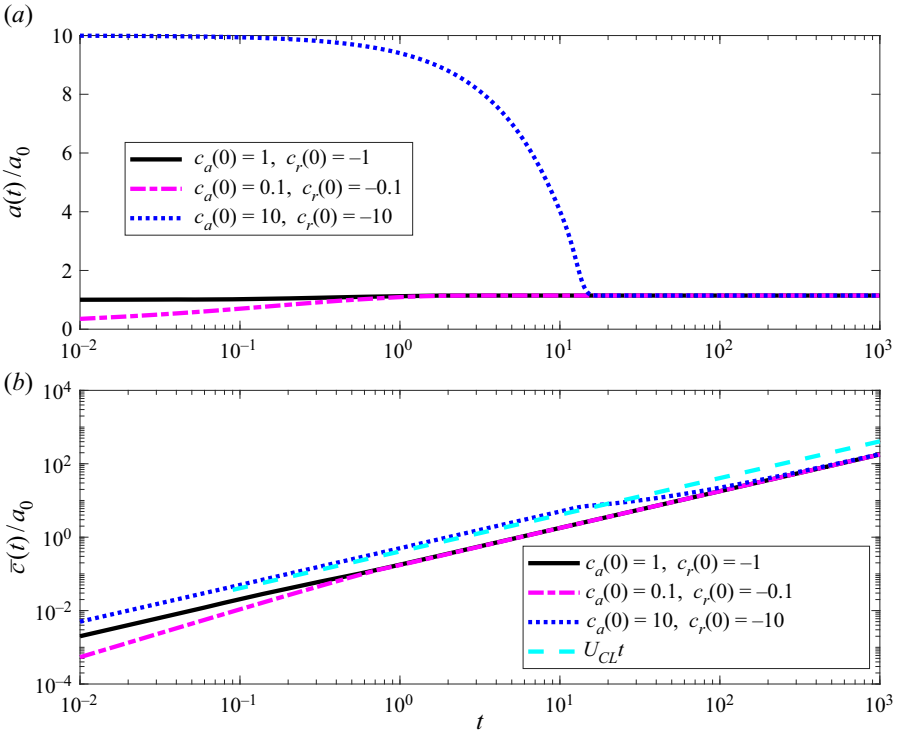

Figure 8. (*a*) Time evolution of dimensionless droplet radius $a(t)/a_0$ by solving (3.18*a*,*b*) with contact angles taken from (4.23) and (4.24) for the case of immobile particles at the liquid–solid interface. Here, $3\alpha\mathcal{N}/4 = 1$, $m = 1$ and $(\bar{\theta}_A - \bar{\theta}_R)/\theta_0 = 0.1$. Independent of initial data, the radius converges to a fixed width $a(t)/a_0 = 1.14562$. (*b*) Time evolution of dimensionless droplet midpoint $\bar{c}(t)/a_0$. Independent of initial data, the midpoint acquires a slope proportional to U_{CL}, the latter denoting the theoretical value of the dimensionless migration velocity that we derive in (4.26) evaluated at the fixed point attained asymptotically by the radius $a(t)/a_0 \sim 1.14562$ in (*a*). Similar behaviour is obtained for the choice of the mobility exponent $m = 3$.

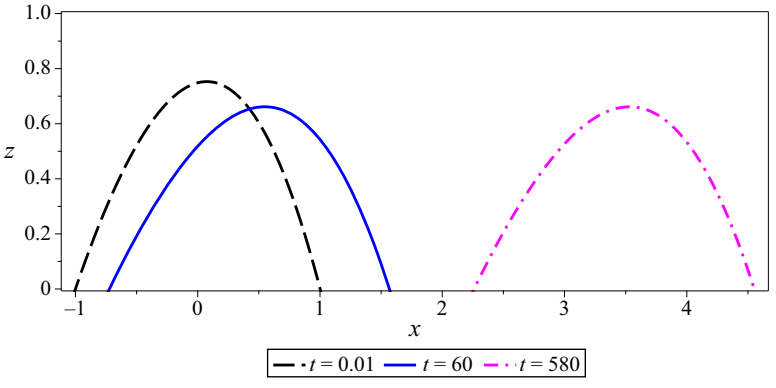

Figure 9. Magnetic droplet profiles migrate on a solid substrate with velocity U_{CL}. The effect is due solely to magnetic torque, where $\frac{3}{4}\alpha\mathcal{N} = 1$. Particle rotation at the liquid–gas interface leads to a left–right asymmetry in the contact angles, migration and a commensurate deformation. The profiles were generated by solving (3.18*a*,*b*) with dynamical contact angles $\theta_a(t)$ and $\theta_r(t)$ from (4.23) and (4.24), and static advancing and receding contact angles $\theta_A = 1.2$ and $\theta_R = 1.1$ (both scaled by the initial contact angle θ_0).

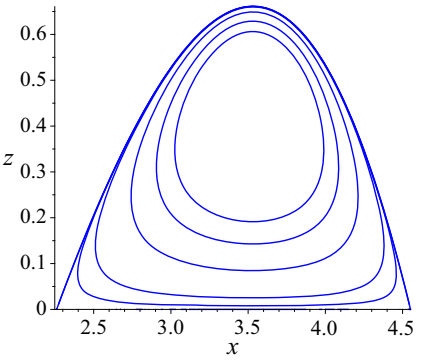

Figure 10. Droplet migration with $\frac{3}{4}\alpha\mathcal{N} = 4$ at time $t = 580$, as displayed in figure 9. The synergy between the magnetic torque and the solid-surface tank-treading embodied in the 'forcing' term $\frac{3}{4}\alpha\mathcal{N}$ of'(4.21) deforms the droplet and its streamlines, breaks the left–right symmetry of the contact angles, and leads to migration with velocity U_{CL} (cf. (4.26)).

with respect to dimensionless and dimensional parameters, respectively, from which one can derive a bound for the necessary torque required to give rise to droplet migration,

$$N > \frac{10\eta'\gamma\,\Delta\theta}{3\zeta a_0^3}, \tag{4.29}$$

by making the simplifying estimate $A \sim 1$, that is, $a \sim a_0$.

Droplet migration takes place when the expression inside the square brackets of (4.26) is positive. This is a transcendental equation that $\mathcal{N}$ has to satisfy in order for migration to take place.

For certain applications, for instance those promoting active surfaces, one will be interested in estimating the liquid velocity at the peak of the interface $z = \xi(x, t)$ (cf. figure 1). Following the same line of argument as at the end of the previous subsection, we arrive at the estimates

$$U_t \sim \frac{7}{24}\,\alpha\bar{\mathcal{N}}\Xi^3 + O(\Xi^5), \quad \text{or} \quad u_t \sim \frac{7}{24}\,\frac{\zeta}{(\eta+\zeta)\eta'}\,N\xi^3 + O(\xi^5) \tag{4.30}$$

in the limit of small droplet thickness.

In figure 11, we display droplet snapshots taken at various regimes formed in the $A, \mathcal{N}$ plane. The interpretation of the various regimes is given in figure 11(*b*). Pure migration (without spreading or receding contact angles) takes place at the central line $\theta_a(t) - \bar{\theta}_A = -\theta_r(t) + \bar{\theta}_R$, for all marked torque values, from its intersection with the $\theta_a = \bar{\theta}_A$ and $\theta_r(t) = \bar{\theta}_R$ curves to its intersection with the $\theta_r(t) = 0$ curve.

5. Droplet migration against fields: the inclined substrate

Interfacial driving mechanisms are particularly important in microfluidic devices due to their large surface-to-volume ratio. Current interest lies in discrete or continuous microscopic control of small-scale systems, and applications vary from clinical and forensic analysis to semiconductor devices and environmental monitoring (Darhuber & Troian 2005).

An immediate application can be found in actuating droplets against fields and forces. For instance, the mechanism described in the present paper can be employed to drive

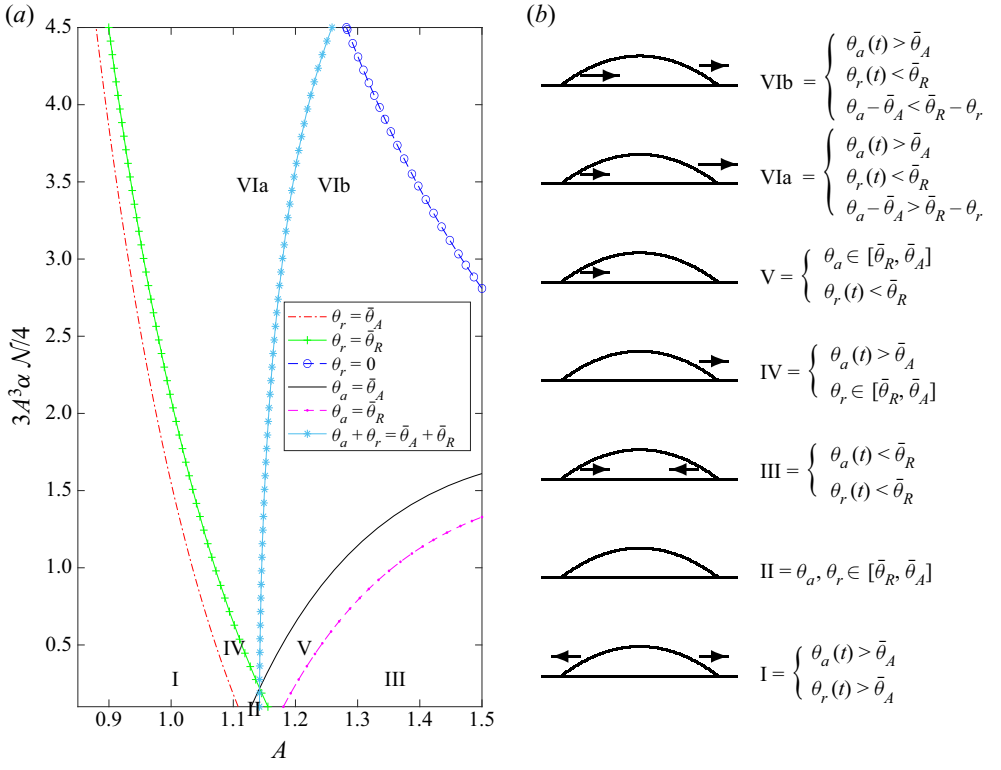

Figure 11. Parameter plot for dimensionless droplet radius $A = c_a(t) - c_r(t)/2a_0$ versus dimensionless torque $\frac{3}{4}\alpha\mathcal{N} = 3\lambda\zeta a_0^3 N/(\eta'\gamma)$ (cf. (4.21)) for the evolution of the droplet with static advancing and receding contact angles $\bar{\theta}_A = 1.2$ and $\bar{\theta}_R = 1.1$ (scaled by θ_0), employing (4.23) and (4.24). The seven allowed regions describe: I, two-sided spreading; II, pinned (immobile) droplet; III, receding droplet; IV, pinned left, spreading right contact line; V, pinned right, receding left contact line; VIa, droplet migrates and spreads; VIb droplet migrates and recedes. The delineations correspond to $\theta_r(t) = \bar{\theta}_A$, $\theta_r(t) = \bar{\theta}_R$, $\theta_r(t) = 0$, $\theta_a(t) = \bar{\theta}_A$, $\theta_a(t) = \bar{\theta}_R$, $\theta_a(t) - \bar{\theta}_A = -\theta_r(t) + \bar{\theta}_R$. The upper right corner region of the plot (above the line $\theta_r = 0$) corresponds to unphysical behaviour.

droplets against the gravitational field: pressure gradients will be balanced against gravity when droplets climb a plane inclined at an angle ψ (cf. figure 1*b*).

5.1. *Infinitesimally inclined substrate*

We recall from (4.4) that $\bar{C}\bar{P}_X = G(\sin\psi/\theta_0 + \Xi_X\cos\psi) - \Xi_{XXX}$. Assuming small inclination angles $\psi = \theta_0\psi_0$ (small θ_0, finite ψ_0), the perpendicular and horizontal components of gravity involve

$$G\cos\psi \sim G \quad \text{and} \quad \frac{G}{\theta_0}\sin\psi \sim G\psi_0, \tag{5.1a,b}$$

respectively. Thus the quasi-static profile of the liquid–gas interface is given (for $\Lambda \neq 0$) by

$$\Xi_{XXX} - G\Xi_X + 3\alpha\Lambda\mathcal{N} - \psi_0 G \sim 0. \tag{5.2}$$

This is the same as the equation describing the quasi-static evolution of droplets with finite particle angular velocity at the liquid–solid substrate interface (cf. (4.5)) corrected for the

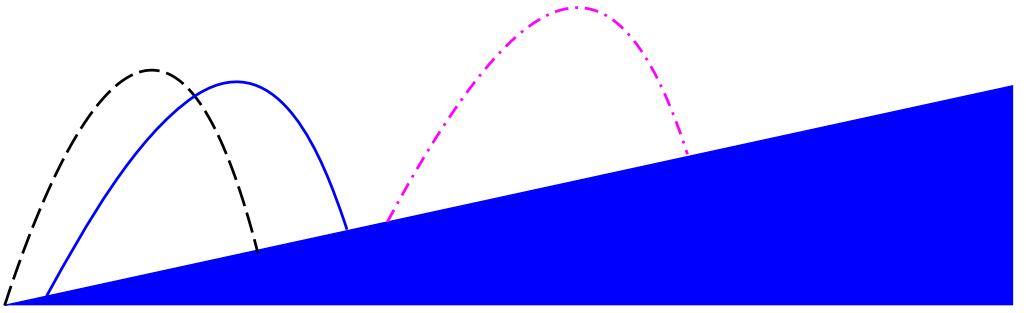

Figure 12. Droplet profiles at times $t = 0.1$, 12 and 80 from left to right. The combined effect of bulk magnetic torque and tank-treading at the liquid–solid interface induces droplet migration on an inclined substrate with $G \sin\psi = 0.1$, $3\alpha\Lambda\mathcal{N} = 4$. Their effect leads to a left–right asymmetry in the contact angles, a commensurate deformation that, when contact angles overcome hysteresis effects (see (5.4)), will lead the droplets to act against the gravitational field, thus starting to climb the inclined plane.

presence of finite inclination $\psi_0 G$. Thus the results of § 4.2 carry over here by making the substitution

$$3\alpha\Lambda\mathcal{N} \to 3\alpha\Lambda\mathcal{N} - \psi_0 G. \tag{5.3}$$

In particular, the droplet migration velocity is given by

$$U_{CL} = \left[(3\alpha\Lambda\mathcal{N} - \psi_0 G)\, \frac{A\sqrt{G}\cosh A\sqrt{G} - \sinh A\sqrt{G}}{G\sinh A\sqrt{G}} - \frac{\bar{\theta}_A - \bar{\theta}_R}{2} \right]^m. \tag{5.4}$$

Figure 12 displays droplets climbing an inclined plane at small angle $\theta_0\psi_0$ with velocity U_{CL} (cf. (5.4)) whose profiles are calculated from (4.7) by incorporating the contact angles (4.9) into the mobility law (3.18*a*,*b*) and performing the substitution (5.3). Thus the magnetic torque-induced deformation of the droplet leads to a left–right asymmetry of the contact angles that overcomes both hysteresis effects (at a sufficiently strong magnitude of the torque) and the decelerating effects of gravity. The propulsion mechanism described in this paper can be employed to drive droplets against other fields, such as temperature gradients.

6. Climbing films

The evolution equation with flux function (3.38) that incorporates the effects of finite particle angular velocity ($\Lambda \neq 0$) at the liquid–solid interface can be employed to realize the climbing of magnetic films on an incline (cf. figure 1*c*). There are two physical effects at play here: the magnetic torque itself generates a 'conveyor-belt' type mechanism induced by the particle collective rotation at the liquid–gas interface, which can enable transport of cargo. On the other hand, the finite particle angular velocity at the liquid–solid interface acts as 'tank-treading' that enables the whole film to climb.

If such a mechanism is to be used for the transport of cargo, then one would need to know the order of magnitude of the 'conveyor-belt' velocity. The liquid velocity field will again be given by (A1), employing the alternative scalings (cf. Kirkinis 2017)

$$U = \frac{u}{U_0}, \quad \Xi = \frac{\xi}{\xi_0}, \quad \Lambda = \frac{\lambda}{\xi_0}, \quad \bar{\mathcal{N}} = \frac{N\xi_0^2}{\eta'\Omega_0}, \quad \alpha = \frac{\zeta}{\eta+\zeta}, \quad \beta = 2\,\frac{\zeta\xi_0^2}{\eta'}, \tag{6.1a–f}$$

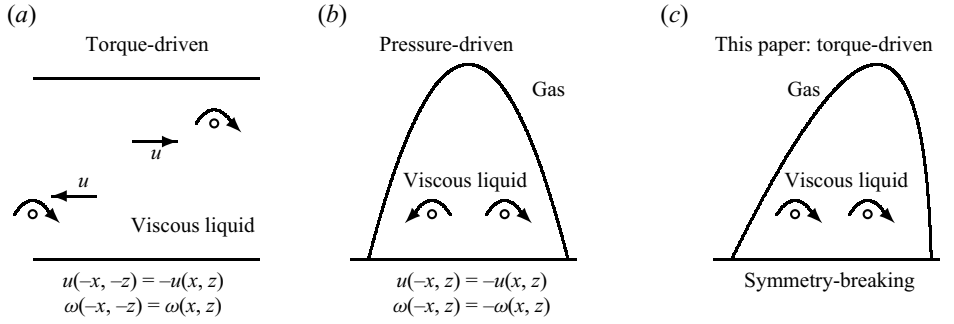

Figure 13. Symmetries of the equations of motion for (*a*) a torque-driven (hard-wall) channel flow, (*b*) a pressure-driven droplet, and (*c*) symmetry-breaking in a torque-driven droplet. See the text for discussion of (*c*) (developed in the present paper).

where ξ_0, U_0 and $\Omega_0 = U_0/\xi_0$ are the characteristic thickness, horizontal velocity and particle angular velocity of the film. We consider the quasi-static limit for which $\bar{C} \to 0$.

The interfacial velocity is thus given in the two separate regimes

$$U_t \sim \frac{1}{2}\alpha\Lambda\bar{\mathcal{N}}\Xi^2, \quad \text{or} \quad u_t \sim \frac{\lambda\zeta}{2\eta'(\eta+\zeta)}N\xi^2, \quad \text{for } \Lambda \neq 0, \tag{6.2}$$

and

$$U_t \sim \frac{7}{24}\alpha\bar{\mathcal{N}}\Xi^3, \quad \text{or} \quad u_t \sim \frac{7\zeta}{24\eta'(\eta+\zeta)}Nh\xi^3, \quad \text{for } \Lambda = 0. \tag{6.3}$$

Thus, under this mechanism, the transport of cargo (cf. figure 1) is a possibility.

7. Droplet migration is induced by symmetry-breaking

When a magnetic liquid moves in a channel under the influence of a magnetic torque N, the equations of motion (3.6)–(3.8) and the corresponding boundary conditions (3.12*a*,*b*) and (3.14) are invariant with respect to the transformation (cf. figure 13*a*)

$$(x, z) \to (-x, -z), \quad (u, w) \to (-u, -w), \quad \omega \to \omega, \tag{7.1a–c}$$

where the latter two symmetries are present because the velocity is a polar vector and the angular velocity is an axial or pseudo-vector, and the gravitational potential is ignored. A similar symmetry ($x \to -x$, $u \to -u$, $\omega \to -\omega$) holds for a magnetic liquid in a droplet in the presence of a pressure gradient but in the absence of an external field (magnetic torque or temperature gradient); see figure 13(*b*).

In this paper, we consider the case displayed in figure 13(*c*). A droplet in the presence of a magnetic torque breaks the reflection symmetry $x \to -x$, whereby ω and its derivatives become the symmetry-breaking terms in the equations of motion (3.6)–(3.8) and in the shear stress boundary condition (first equation of (3.12*a*,*b*)). The loss of symmetry in the above system is inherited by the evolution equation for the liquid–gas interface,

$$\xi_t + N\left(\xi^n\right)_x + \left[\xi^3(-g\xi_x + \gamma\xi_{xxx})\right]_x = 0, \tag{7.2}$$

written in a form suggestive only of the physical effects by scaling the numerical factors, and where n is a positive integer (cf. (3.40) and (3.41)). Here, N is the magnetic torque or

the strength of a surface tension gradient induced by a horizontal temperature gradient (Smith 1995), g is the gravitational acceleration, and γ is the surface tension. In the analysis of the thermocapillary droplet migration, Smith (1995) found the exponent $n = 2$. Here, we consider problems described by equations more general than (7.2), but in certain limits, our problem can be reduced to equations of the type (7.2), so one can explore the physics of droplet migration by this simple model. In these simplifying cases, we find the exponents $n = 3$ (when a finite particle angular velocity is allowed at the liquid–solid interface, $\lambda \neq 0$ in (3.10*a–c*); see (3.40)) and $n = 4$ (when $\lambda \equiv 0$; see (3.41)).

In the absence of external torque, (7.2) is invariant with respect to the reflection symmetry $x \to -x$. The torque N breaks this symmetry. For a thin long film, and in the presence of an instability mechanism (Rayleigh–Taylor instability, thermocapillary instability, attractive van der Waals intermolecular forces, etc.), it was shown (Kirkinis & Davis 2015) that the loss of this symmetry leads to a unidirectional nonlinear interfacial wave propagation that can mitigate the effects of instability. The unidirectional character of (7.2) comes from the single time derivative, and the nonlinearity (convective term multiplying N) gives rise to shock or rarefaction waves that, however, become smoothed out by surface-tension-mediated dispersion (the term multiplying γ) and by gravity.

A droplet is, however, characterized by the absorbing boundaries (3.37*a*,*b*) that limit wave propagation. Thus the consequence of the symmetry-breaking nonlinear term multiplying N in (7.2), or the symmetry-breaking that equivalently takes place in the original equations (3.6)–(3.8) coupled to the shear stress boundary conditions (first of (3.12*a*,*b*)), is to induce a permanent non-axisymmetric deformation of the droplet.

The effects of symmetry breaking are also inherited by the mobility law (3.18*a*,*b*). In the absence of torque (but in the presence of gravity or a vertical temperature gradient with a Marangoni number denoted by M; Ehrhard & Davis 1991), the midpoint of the droplet is immobile:

$$\frac{\mathrm{d}(c_a + c_r)}{\mathrm{d}t} = 0. \tag{7.3}$$

This is because in the cases considered by Ehrhard & Davis (1991), the left and right dynamic contact angles are equal to each other ($\theta_a = -h_x(c_a) = h_x(c_r) = \theta_r$) and the droplet can undergo only spreading or retraction. Analytically,

$$\frac{\mathrm{d}(c_a + c_r)}{\mathrm{d}t} = (\theta_a(M) - \bar{\theta}_A)^m - (\theta_r(M) - \bar{\theta}_A)^m \sim m(\theta_a(0) - \bar{\theta}_A)^{m-1} M \left(\frac{\mathrm{d}\theta_a}{\mathrm{d}M} - \frac{\mathrm{d}\theta_r}{\mathrm{d}M} \right) = 0 \tag{7.4}$$

because $\mathrm{d}\theta_a/\mathrm{d}M = \mathrm{d}\theta_r/\mathrm{d}M$; see figure 14(*a*) and the mobility law (3.18*a*,*b*) – in this calculation, we considered the approximation $\theta_a(M) \sim \theta_a(0) + M(\mathrm{d}\theta_a/\mathrm{d}M)(0)$, $\theta_r(M) \sim \theta_r(0) + M(\mathrm{d}\theta_r/\mathrm{d}M)(0)$ and the fact that $\theta_a(0) = \theta_r(0)$.

In the presence of torque that we are considering in this paper (or a horizontal temperature gradient considered by Smith (1995), both denoted by N) we show that the droplet midpoint is instead mobile:

$$\frac{\mathrm{d}(c_a + c_r)}{\mathrm{d}t} \neq 0. \tag{7.5}$$

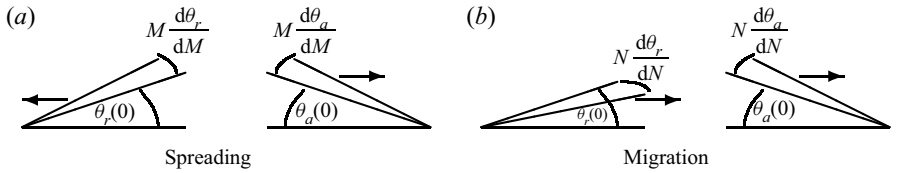

Figure 14. (*a*) Explanation of the calculation of the midpoint velocity of the droplet in (7.4), under a vertical temperature gradient (Ehrhard & Davis 1991). The droplet whose contact angles, in the absence of the temperature gradient, are $\theta_r(M=0)=\theta_a(M=0)$ spreads under the influence of the gradient of strength M. The contact angle increments generated by it are equal: $M(\mathrm{d}\theta_r/\mathrm{d}M)(M=0)=M(\mathrm{d}\theta_a/\mathrm{d}M)(M=0)$. (*b*) Explanation of the calculation of the midpoint velocity of the droplet in (7.6), under a horizontal temperature gradient (Smith 1995) or the magnetic torque (studied in the present paper). The droplet whose contact angles, in the absence of the temperature gradient, are $\theta_r(N=0)=\theta_a(N=0)$ migrates under the influence of the horizontal temperature gradient or magnetic torque (whose strength is denoted by N). The contact angle increments generated by it have equal magnitudes but opposite signs: $N(\mathrm{d}\theta_r/\mathrm{d}N)(N=0)=-N(\mathrm{d}\theta_a/\mathrm{d}N)(N=0)$.

Thus, in contrast to the case of spreading described by (7.4) (Ehrhard & Davis 1991), we now have $\mathrm{d}\theta_a/\mathrm{d}N=-\mathrm{d}\theta_r/\mathrm{d}N$ (see figure 14*b*). Thus

$$\frac{\mathrm{d}(c_a+c_r)}{\mathrm{d}t}=(\theta_a(N)-\bar{\theta}_A)^m+(\bar{\theta}_R-\theta_r(N))^m$$
$$\sim mN(\theta_a(0)-\bar{\theta}_A)^{m-1}\left(\frac{\mathrm{d}\theta_a}{\mathrm{d}N}-\frac{\mathrm{d}\theta_r}{\mathrm{d}N}\right)=2N\frac{\mathrm{d}\theta_a}{\mathrm{d}N}\neq 0, \tag{7.6}$$

where in the last equality we set $m=1$. Thus symmetry-breaking, evident in the Navier–Stokes equations, its various reductions and constitutive laws, accompanies the migration of liquid droplets.

8. Estimates

In this section, we provide numerical estimates of the effects discussed in this paper. Various magnetic torque density experimental measurements have appeared in the literature, ranging from 0.3 dyne cm^{-2} to 2×10^4 dyne cm^{-2}. In table 2, we take the middle of these values to use as a characteristic torque density.

For the non-zero particle angular velocity at the liquid–solid substrate case, developed in § 4.2, from (4.19) and employing values from table 2, we calculate $\eta'\gamma(\bar{\theta}_A-\bar{\theta}_R)/6\zeta\lambda a^2\sim 2$, which provides a conservative estimate of the required magnetic torque that leads to droplet migration. This estimate is much lower than characteristic experimental torque measurements (see table 2 and Chaves *et al.* 2008), demonstrating that the theory that we developed in the foregoing sections is compatible with experiment.

A similar estimate can be carried out for the zero particle angular velocity at the liquid–solid substrate case, developed in § 4.3. Equation (4.29), $10\eta'\gamma\,\Delta\theta/3\zeta a_0^3\sim 9$, shows that this value is also compatible with experimental torque measurements (see table 2 and Chaves *et al.* 2008).

The contact line velocity depends on the mobility k and the deviation of N away from $\Delta\theta$. The phenomenological constant k also has to be determined by experiment. For instance, Ehrhard (1993) determined that $k\sim 4$ mm s^{-1} and $k\sim 8$ mm s^{-1} for silicon oil and paraffin oil, respectively, in his experiments on non-isothermal spreading on glass.

Quantity	Description	Definition
$\bar{\theta}_A, \bar{\theta}_R$	Static advancing and receding contact angles	figure 2, (3.19*a*,*b*)
$\theta_a(t), \theta_r(t)$	Right and left dynamic contact angles	figure 2, (3.17*a*,*b*)
η, ζ, η'	Constitutive parameters	(2.2), (2.4)
$c_a(t), c_r(t)$	Horizontal coordinates of right/left contact lines	(3.17*a*,*b*)
$a(t), A(t)$	Dimensional (-less) droplet half-width (radius)	(A8), (4.8)
$\bar{c}(t)$	Dimensional centre of the droplet	(A6)
$u, w, (U, W)$	Dimensional (-less) horizontal/vertical velocity fields	(3.2*a–c*), (3.22*a–e*)
$u_{CL}, (U_{CL})$	Dimensional (-less) contact line velocity	(1.1), (3.22*a–e*)
$\omega, (\Omega)$	Dimensional (-less) particle angular velocity	(3.8), (3.22*a–e*)
m, h, b	Dimensional magnetization and magnetic fields	(2.5*a*,*b*)
$\lambda, (\Lambda)$	Dimensional (-less) rotational slip length	(2.14), (3.23*a–d*)
k	Contact line mobility	(1.1)
$\mathcal{K}$	Mean curvature	(2.9), (3.13)
$\hat{\boldsymbol{t}}, \hat{\boldsymbol{n}}$	Tangent and normal unit vectors at an interface	figure 2, (2.9), (3.11*a*,*b*)
$x, z, t, (X, Z, T)$	Dimensional (-less) spatial coordinates and time	figure 2, (3.21*a–c*)
$\xi(x, t), (\Xi(X, T))$	Dimensional (-less) liquid–gas interface	(3.22*a–e*), (3.1)
θ_0, a_0, V_0	Characteristic contact angle/droplet radius/volume	(3.21*a–c*), (3.37*a*,*b*), (3.20*a–c*)
τ_B, ν	Brownian time scale and external field frequency	(2.7)
$p, (P)$	Dimensional (-less) pressure	(2.2), (3.22*a–e*)
Re, Re'	Translational and rotational Reynolds numbers	(3.23*a–d*)
$\bar{C}$	Capillary number	(3.23*a–d*)
$N, (\bar{\mathcal{N}}, \mathcal{N})$	Dimensional (-less) magnetic torque	(2.6), (3.24*a*,*b*), (4.1*a*,*b*)
$g, (\bar{G}, G)$	Dimensional (-less) grav. acceleration, Bond number	(3.9), (3.26*a*,*b*), (4.1*a*,*b*)
$\phi, (\Phi)$	Dimensional (-less) potential	(3.9), (3.24*a*,*b*), (3.26*a*,*b*)
Ψ	Dimensionless streamfunction	(4.11)
ψ	Inclination angle of a plane	§ 5

Table 1. Notation employed in this paper.

Quantity	Value	Definition
$\bar{\theta}_A - \bar{\theta}_R$ (deg.)	10–20	Hysteresis angle
η (g cm^{-1} s^{-1})	0.045	Viscosity (2.2)
ζ (g cm^{-1} s^{-1})	0.003	Vortex viscosity (2.2)
η' (g cm s^{-1})	10^{-7}	Spin viscosity (2.4)
γ (dyne cm^{-1})	29	Surface tension
a_0 (cm)	5×10^{-2}	Characteristic droplet radius
θ_0 (deg.)	3–10	Characteristic initial angle
ξ (cm)	2×10^{-3}	Droplet maximum thickness
N (dyne cm^{-2})	2	Characteristic torque density
λ (cm)	10^{-2}	Rotational slip length (2.14)

Table 2. Experimental values taken from Rinaldi & Zahn (2002) and Chaves *et al.* (2006, 2008) for EMG 900_2 ferrofluid and from Ehrhard (1993).

An estimate of the velocity of cargo transport (6.3) by a climbing film is

$$u_t \sim \frac{7\zeta}{24\eta'(\eta+\zeta)} N\xi^3 \sim 30\ \mu\text{m s}^{-1}, \tag{8.1}$$

following the values of table 2.

9. Discussion

In this paper, we demonstrated the effectiveness of a magnetic torque in a liquid endowed with rotational degrees of freedom to induce migration of liquid droplets: the collective particle rotation at the droplet free surface, acting as a surface shear, can overcome hysteresis effects and lead to their migration even in the presence of opposing external fields. We obtained non-perturbative expressions for the droplet migration velocity and other observables that could be incorporated easily in an experiment.

It was discussed recently that a liquid with broken time-reversal symmetry allows for the incorporation of new stress and rate-of-strain relations into the liquid constitutive laws (Ganeshan & Abanov 2017). At a liquid–gas interface, the stress accompanying odd viscosity is always normal to the standard shear stress of Newtonian liquids. This can bring about new effects. For instance, the particle-angular-velocity-induced shear stress giving rise to the effects studied in the present paper will be accompanied by an odd viscosity-induced normal pressure (Avron 1998). This could influence the shape of the droplet and its dynamics. Investigation of such effects is beyond the scope of the present paper. See Kirkinis, Mason & Olvera de la Cruz (2022) for a discussion of the consequences of odd viscosity on free-surface flows.

Although the effect discussed in the present paper has definite applications in industry (cf. figure 1), its inspiration originates from medicine. In particular, it is based on the observation that targeting malignant cells with nanoparticles has proven elusive: recent research showed that only 1 % of these particles reach their target (Wilhelm *et al.* 2016). The ramifications of this failure include poor translation of nanotechnology to humans, increased costs and toxicity, and declining therapeutic efficacy. To digress from the 1 % targeting threshold, it is imperative that new and unconventional mechanisms of locomotion are invented. Thus our work in the present paper should be considered as a precursor to the development of future targeting-specific locomotion strategies.

Acknowledgements. This paper is dedicated to the memory of Stephen H. Davis (7 September 1939–12 November 2021), colleague and friend. The authors are grateful to the anonymous referees for their comments and criticism that improved the manuscript.

Funding. This work was supported by the Center for Bio-Inspired Energy Science (CBES), an Energy Frontier Research Center funded by the US Department of Energy (DOE) Office of Basic Energy Sciences (DE-SC0000989). Funding was also obtained from the Fairchild Foundation through the Center for Computation & Theory of Soft Materials at Robert R. McCormick School of Engineering and Applied Science, Northwestern University.

Declaration of interests. The authors report no conflict of interest.

Author ORCIDs.
A. Aggarwal https://orcid.org/0000-0002-4008-4451;
E. Kirkinis https://orcid.org/0000-0002-1140-9632;
M. Olvera de la Cruz https://orcid.org/0000-0002-9802-3627.

Appendix A. U and Ω for constant torque

In the lubrication approximation, the liquid velocity and particle angular velocities (already satisfying $U_Z = 2\alpha\Omega$, at $Z = \Xi(X, T)$, and $U = 0$ at $Z = 0$) take the forms

$$U = \frac{(1/2z^2 - Hz)\bar{P}_X}{1-\alpha} + \frac{\alpha\bar{\mathcal{N}}z}{\beta(1-\alpha)} + 2\,\frac{\alpha\left(C_1(\mathrm{e}^{\kappa z} - 1) - C_2(\mathrm{e}^{-\kappa z} - 1)\right)}{k}, \tag{A1}$$

$$\Omega = \frac{\bar{P}_X(z-H)}{2-2\alpha} + C_1\,\mathrm{e}^{\kappa z} + C_2\,\mathrm{e}^{-\kappa z} + \frac{1}{2}\frac{\bar{\mathcal{N}}}{\beta\ (1-\alpha)} \tag{A2}$$

where the constants C_i are determined from the boundary conditions

$$\Omega = 0 \text{ at } Z = \Xi(X,T) \quad \text{and} \quad \Omega = \Lambda\Omega_Z \text{ at } Z = 0. \tag{A3a,b}$$

as

$$C_1 = -\frac{\left(\Xi\,\mathrm{e}^{-\kappa\Xi}\,\kappa + \Lambda\,\mathrm{e}^{-\kappa\Xi}\,\kappa - \Lambda\kappa - 1\right)\bar{P}_X}{2\left(\Lambda\kappa\,\mathrm{e}^{\kappa\Xi} - \Lambda\,\mathrm{e}^{-\kappa\Xi}\,\kappa + \mathrm{e}^{\kappa\Xi} + \mathrm{e}^{-\kappa\Xi}\right)\kappa(\alpha-1)} + \frac{\bar{\mathcal{N}}\,\mathrm{e}^{-\kappa\Xi}}{2(\alpha-1)\left(\Lambda\kappa\,\mathrm{e}^{\kappa\Xi} - \Lambda\,\mathrm{e}^{-\kappa\Xi}\,\kappa + \mathrm{e}^{\kappa\Xi} + \mathrm{e}^{-\kappa\Xi}\right)\beta} \tag{A4}$$

and

$$C_2 = -\frac{\left(\Xi\,\mathrm{e}^{\kappa\Xi}\,\kappa + \Lambda\kappa\,\mathrm{e}^{\kappa\Xi} - \Lambda\kappa + 1\right)\bar{P}_X}{2\left(\Lambda\kappa\,\mathrm{e}^{\kappa\Xi} - \Lambda\,\mathrm{e}^{-\kappa\Xi}\,\kappa + \mathrm{e}^{\kappa\Xi} + \mathrm{e}^{-\kappa\Xi}\right)\kappa(\alpha-1)} + \frac{\mathrm{e}^{\kappa\Xi}\,\bar{\mathcal{N}}}{2(\alpha-1)\left(\Lambda\kappa\,\mathrm{e}^{\kappa\Xi} - \Lambda\,\mathrm{e}^{-\kappa\Xi}\,\kappa + \mathrm{e}^{\kappa\Xi} + \mathrm{e}^{-\kappa\Xi}\right)\beta}. \tag{A5}$$

A.1. *Formulation in the 'centre-of-mass' frame of reference*

Following Smith (1995), we can formulate the problem by considering the droplet moving with respect to the reference frame whose origin is located at the centre of the droplet:

$$\bar{c}(t) = \frac{c_a(t) + c_r(t)}{2}. \tag{A6}$$

Then we define a new coordinate X with respect to the new origin and a new droplet height $\bar{\xi}(\bar{x})$ such that

$$\bar{x} = x - \bar{c}(t) \quad \text{and} \quad \bar{\xi}(\bar{x}) = \bar{\xi}(x - \bar{c}(t)) = \xi(x) = \xi(\bar{x} + \bar{c}(t)). \tag{A7a,b}$$

Defining the half-width of the droplet as

$$a(t) = \frac{c_a(t) - c_r(t)}{2}, \tag{A8}$$

we have, for example, $\bar{\xi}_{\bar{x}}(a) = \xi_x(c_a)$ and $\bar{\xi}_{\bar{x}}(-a) = \xi_x(c_r)$. Then the boundary conditions become

$$\bar{\xi}(-a) = \bar{\xi}(a) = 0, \quad 1 = \int_{-a}^{a} \bar{\xi}(\bar{x})\,\mathrm{d}\bar{x}, \tag{A9a,b}$$

with

$$\theta_a(t) = -\bar{\xi}_{\bar{x}}(a), \quad \theta_r(t) = \bar{\xi}_{\bar{x}}(-a). \tag{A10a,b}$$

One then needs to integrate (3.18*a*,*b*) with the above boundary conditions to obtain c_a and c_r, and from them obtain expressions for the half-width $a(t)$ and droplet centre $\bar{c}(t)$.

We will invoke two simplifications in the notation. First, we drop the bars on the variables defined in this section. And second, we will scale the static angles $\bar{\theta}_A$ and $\bar{\theta}_R$, and their dynamic counterparts $\theta_a(t)$ and $\theta_r(t)$, by the initial angle θ_0. For notational simplicity, we will retain the same symbol for both unscaled and scaled angles.

Appendix B. General expression for migration velocity in the perturbative regime

We recall that in the case of thermocapillary spreading of a viscous droplet (Ehrhard & Davis 1991), the left and right contact lines are simultaneously advancing or receding. Without loss of generality, we consider only the advancing case (as was developed in the thermocapillarity problem; Ehrhard & Davis 1991): the left and right contact angles are always equal, so

$$\theta_a = F_0 + MF_1 \quad \text{and} \quad \theta_r = F_0 + MF_1, \tag{B1a,b}$$

where $F_0 = -3/(2a^2)$, $F_1 = 3a/2$, $M \ll 1$ is the Marangoni number (proportional to the temperature gradients responsible for the spreading behaviour), and $a = a(t)$ is the droplet spreading radius. The smallness of the parameter M implies that the above result holds in a perturbative calculation, or when the external effects that lead to motion can be superposed on a base motion (as is the case in the non-perturbative result that we derive in § 4.2).

On the other hand, in the presence of a horizontal temperature gradient (Smith 1995) or torque of strength $\bar{\mathcal{N}}$ (considered in the present paper), the left–right symmetry of contact angles breaks

$$\theta_a = F_0 + \bar{\mathcal{N}}F_1 \quad \text{and} \quad \theta_r = F_0 - \bar{\mathcal{N}}F_1. \tag{B2a,b}$$

The explicit forms of F_0 and F_1 are not needed here; in the context of a specific problem, they are given, for instance, by (4.16*a–c*). When the droplet has reached its steady-state migration shape and velocity (i.e. moving as a whole without deforming and at constant speed), the contact angles are related by

$$\theta_a - \bar{\theta}_A = \bar{\theta}_R - \theta_r \quad \text{and} \quad \theta_a - \bar{\theta}_A > 0, \quad \theta_r \geqslant 0 \tag{B3a,b}$$

(cf. the central vertical curve in figures 6, 7 and 11). Employing (B2*a*,*b*), the above expressions lead to

$$\theta_a + \theta_r = 2F_0 = \bar{\theta}_A + \bar{\theta}_R, \tag{B4}$$

and the inequality

$$0 < \tfrac{1}{2}(\bar{\theta}_A - \bar{\theta}_R) < \bar{\mathcal{N}}F_1. \tag{B5}$$

Employing (B4), the migration velocity is then given by

$$U_{CL} = (\theta_a - \bar{\theta}_A)^m = \left[F_0 + \bar{\mathcal{N}}F_1 - \bar{\theta}_A\right]^m = \left[\bar{\mathcal{N}}F_1 - \frac{\bar{\theta}_A - \bar{\theta}_R}{2}\right]^m. \tag{B6}$$

Migration velocities derived in the main body of the present paper in the limit of small $\bar{\mathcal{N}}$ acquire this form (see (4.16*a–c*) and (4.28)). For a specially prepared substrate devoid of hysteresis effects ($\bar{\theta}_A = \bar{\theta}_R \neq 0$), the migration velocity reduces to

$$U_{CL} = \left(\bar{\mathcal{N}}F_1\right)^m, \tag{B7}$$

thus droplet migration is a purely magnetic-torque-induced effect. This discussion is independent of the specific numerical value attached to the exponent m. A direct derivation of (B6) and (B7) can also be carried out.

References

Aero, E.L., Bulygin, A.N. & Kuvshinskii, E.V. 1965 Asymmetric hydromechanics. *Z.. Angew. Math. Mech.* **29** (2), 333–346.

Avron, J.E. 1998 Odd viscosity. *J. Stat. Phys.* **92** (3–4), 543–557.

Chaves, A. & Rinaldi, C. 2014 Interfacial stress balances in structured continua and free surface flows in ferrofluids. *Phys. Fluids* **26** (4), 042101.

Chaves, A., Rinaldi, C., Elborai, S., He, X. & Zahn, M. 2006 Bulk flow in ferrofluids in a uniform rotating magnetic field. *Phys. Rev. Lett.* **96** (19), 194501.

Chaves, A., Zahn, M. & Rinaldi, C. 2008 Spin-up flow of ferrofluids: asymptotic theory and experimental measurements. *Phys. Fluids* **20** (5), 053102.

Condiff, D.W. & Dahler, J.S. 1964 Fluid mechanical aspects of antisymmetric stress. *Phys. Fluids* **7** (6), 842–854.

Dahler, J.S. & Scriven, L.E. 1961 Angular momentum of continua. *Nature* **192**, 36–37.

Darhuber, A.A. & Troian, S.M. 2005 Principles of microfluidic actuation by modulation of surface stresses. *Annu. Rev. Fluid Mech.* **37**, 425–455.

Davis, M.J., Gratton, M.B. & Davis, S.H. 2010 Suppressing van der Waals driven rupture through shear. *J. Fluid Mech.* **661**, 522–539.

Davis, S.H. 2002 Interfacial fluid dynamics. In *Perspectives in Fluid Dynamics: A Collective Introduction to Current Research* (ed. G.K. Batchelor, H.K. Moffatt & M.G. Worster), pp. 1–51. Cambridge University Press.

Driscoll, M. & Delmotte, B. 2019 Leveraging collective effects in externally driven colloidal suspensions: experiments and simulations. *Curr. Opin. Colloid Interface Sci.* **40**, 42–57.

Dussan, E.B. V 1979 On the spreading of liquids on solid surfaces: static and dynamic contact lines. *Annu. Rev. Fluid Mech.* **11** (1), 371–400.

Ehrhard, P. 1993 Experiments on isothermal and non-isothermal spreading. *J. Fluid Mech.* **257**, 463–483.

Ehrhard, P. & Davis, S.H. 1991 Non-isothermal spreading of liquid drops on horizontal plates. *J. Fluid Mech.* **229**, 365–388.

Ganeshan, S. & Abanov, A.G. 2017 Odd viscosity in two-dimensional incompressible fluids. *Phys. Rev. Fluids* **2** (9), 094101.

de Gennes, P.G. 1985 Wetting: statics and dynamics. *Rev. Mod. Phys.* **57** (3), 827.

Greenspan, H.P. 1978 On the motion of a small viscous droplet that wets a surface. *J. Fluid Mech.* **84** (1), 125–143.

Hoffman, R.L. 1975 A study of the advancing interface. I. Interface shape in liquid–gas systems. *J. Colloid Interface Sci.* **50** (2), 228–241.

Kirkinis, E. 2017 Magnetic torque-induced suppression of van-der-Waals-driven thin liquid film rupture. *J. Fluid Mech.* **813**, 991–1006.

Kirkinis, E. & Davis, S.H. 2013 Hydrodynamic theory of liquid slippage on a solid substrate near a moving contact line. *Phys. Rev. Lett.* **110**, 234503.

Kirkinis, E. & Davis, S.H. 2014 Moffatt vortices induced by the motion of a contact line. *J. Fluid Mech.* **746**, R3.

Kirkinis, E. & Davis, S.H. 2015 Stabilization mechanisms in the evolution of thin liquid-films. *Proc. R. Soc. Lond.* A **471**, 20150651.

Kirkinis, E., Mason, J. & Olvera de la Cruz, M. 2022 Odd viscosity-induced passivation of Moffatt vortices. *J. Fluid Mech.* **950**, A19.

Lauga, E., Brenner, M.P. & Stone, H.A. 2007 Microfluidics: the no-slip boundary condition. In *Springer Handbook of Experimental Fluid Mechanics* (ed. C. Tropea, A.L. Yarin & J.F. Foss), pp. 1219–1240. Springer.

Li, C., *et al.* 2020 Fast and programmable locomotion of hydrogel-metal hybrids under light and magnetic fields. *Sci. Rob.* **5** (49), eabb9822.

Ngan, C.G. & Dussan V, E.B. 1989 On the dynamics of liquid spreading on solid surfaces. *J. Fluid Mech.* **209**, 191–226.

Oron, A., Davis, S.H. & Bankoff, S.G. 1997 Long-scale evolution of thin liquid films. *Rev. Mod. Phys.* **69** (3), 931–980.

Rinaldi, C. 2002 Continuum modeling of polarizable systems. PhD thesis, Massachusetts Institute of Technology.

Rinaldi, C. & Zahn, M. 2002 Effects of spin viscosity on ferrofluid flow profiles in alternating and rotating magnetic fields. *Phys. Fluids* **14** (8), 2847–2870.

Schwartz, A.M. & Tejada, S.B. 1972 Studies of dynamic contact angles on solids. *J. Colloid Interface Sci.* **38** (2), 359–375.

SMITH, M.K. 1995 Thermocapillary migration of a two-dimensional liquid droplet on a solid surface. *J. Fluid Mech.* **294**, 209–230.

TANNER, L.H. 1979 The spreading of silicone oil drops on horizontal surfaces. *J. Phys.* D*: Appl. Phys.* **12** (9), 1473–1484.

TORRES-DÍAZ, I. & RINALDI, C. 2014 Recent progress in ferrofluids research: novel applications of magnetically controllable and tunable fluids. *Soft. Matt.* **10** (43), 8584–8602.

WILHELM, S., TAVARES, A.J., DAI, Q., OHTA, S., AUDET, J., DVORAK, H.F. & CHAN, W.C.W. 2016 Analysis of nanoparticle delivery to tumours. *Nat. Rev. Mater.* **1** (5), 16014.

YANG, T., SPRINKLE, B., GUO, Y., QIAN, J., HUA, D., DONEV, A., MARR, D.W.M. & WU, N. 2020 Reconfigurable microbots folded from simple colloidal chains. *Proc. Natl Acad. Sci. USA* **117** (31), 18186–18193.

ZAHN, M. & GREER, D.R. 1995 Ferrohydrodynamic pumping in spatially uniform sinusoidally time-varying magnetic fields. *J. Magn. Magn. Mater.* **149** (1), 165–173.